

**AD-A282 970**

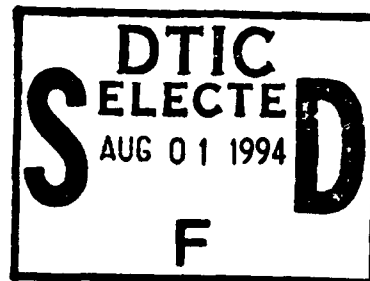


1

**ANALYSIS OF THE THROUGH-THICKNESS  
MICROPORE AND CONSTITUENT PARTICLE  
POPULATION GRADIENTS IN THE 7050-T7451 PLATE  
ALUMINUM ALLOYS**

***Progress Report***

ONR Grant No: N00014-91-J-1299



**Submitted to:**

Dr. A. K. Vasudévan  
Technology Directorate  
Code 4421  
Office of Naval Research  
800 North Quincy Street  
Arlington, VA 22217-5660

**Prepared by:**

This document has been approved  
for public release and sale; its  
distribution is unlimited.

Professor Marek A. Przystupa (Principal Investigator)  
Jimin Zhang  
Annetta J. Luévano  
Department of Materials Science and Engineering  
University of California  
Los Angeles, CA 90024  
Tel.: (310) 825-6559  
FAX: (310) 206-7353

March 1994

**DTIC QUALITY INSPECTED 1**

**94-24088**



**94 7 29 018;**

## CONTENTS

Abstract .....	1
Introduction .....	2
Experimental .....	8
A. Two dimensional size distributions .....	9
B. Three dimensional size distributions .....	11
C. Shapes and alignment .....	13
D. Spatial distributions .....	15
Results and Discussions .....	17
A. Pores .....	17
B. Constituent particles .....	21
C. Spacing and clustering of pores and particles .....	23
Conclusions .....	25
Acknowledgments .....	26
Appendix .....	27
References .....	28
Tables and Figures .....	32

Accession For	
NTIS    CRA&I	<input checked="" type="checkbox"/>
DTIC    TAB	<input type="checkbox"/>
Unannounced	<input type="checkbox"/>
Justification _____	
By _____	
Distribution / _____	
Availability Codes	
Dist	Avail and/or Special
A-1	

## **ABSTRACT**

**This report contains final results of the quantitative characterizations of the pore and constituent particle morphologies in two different variants of the 7050-T7451 six-inch-thick plate alloys. The purpose of those characterizations was to find volume fraction, size, shape and spatial distributions of both phases and their through-thickness gradients. This is the first ever characterization of this scope which provides unavailable until now data necessary for the predictions of the size distributions of the fatigue crack initiating flaws, and for the development and test of all microstructure based fatigue life prediction and durability models. The sizes, shapes, and orientations of both phases were analyzed using the linear intercept method. Their spatial distributions were quantified using the nearest neighbor spacings obtained via Voronoi (Dirichlet) tessellation techniques. Two types of intercept lengths, global and average [5], have been used to represent sizes of both phases on differently oriented test planes and at different locations within the plates. The distributions of those size measures for both features were lognormal. The three dimensional size distributions were also estimated. They were obtained from the characteristics of the computer simulated three dimensional model microstructures which had the same two-dimensional attributes as the two dimensional sections of the real alloy. The analysis of nearest neighbor spacing indicated that both the pores and particles have spatial distributions which can be categorized as random with clusters. In addition, an attempt has been made to use the tessellation cell shapes to identify types of spatial anisotropy of both phases. Results are currently used in the development of the extreme value based methodology for predicting size distributions of the fatigue crack initiating flaws and in the development of the microstructure based stochastic life prediction models.**

## INTRODUCTION

The most important microstructural features controlling mechanical behavior of the engineering alloys, and aluminum alloys in particular, are grains, pores, constituent particles and precipitates. Since the sizes and/or spacings of those features are usually non-uniform, to obtain meaningful correlation between the microstructure and mechanical properties it is necessary to characterize not only the features' average sizes, but also their size and spatial distributions, shapes, orientations and volume fractions. The purpose of this work was to assemble the most efficient quantitative techniques which would facilitate such characterizations and to test them by quantifying microstructural gradients in the 7050-T7451 Al plate alloy. This alloy is known to have microstructural gradients, hence it is an ideal candidate for testing gradient characterization methodologies. The grain structures of the same alloy were previously studied [1] thus the focus of this work was on the characterization of the large second phase dispersions such as pores and the constituent particles.

All characterizations of the second phase dispersions require two types of measurements: (1) the measurements needed for obtaining average individual characteristics, such as size, shape and orientation, and (2) the measurements which give global characteristics, i.e. volume fraction, size and spatial distributions and alignment. The sizes of the second phase dispersions are most conveniently measured using the linear intercept method [1-4]. Obtained size distributions can be then analyzed for conformity with the most common standard distributions, such as normal and lognormal. To describe shapes, various arbitrarily defined shape factors can be used [1-2, 5]. A common problem associated with these factors is that they can have the same values for diametrically different shapes. However, since dispersions in engineering materials have usually similar and relatively simple shapes, their shape differences can be adequately described using the shape factors.

For complex shapes several more precise techniques, such as Fourier and spectral analysis, are also available [6-8]. As to the global properties, the volume fraction can be approximated by the dispersions area fraction measured on plane sections. The alignment can be characterized using one of many measures of the 'degree of orientation' exemplified by the Saltykov's method [9] or by the orientation factor proposed earlier by the authors [5]. The measurements of the spatial distributions of the second phase dispersions will be described in details later on.

All measurements used in this work have been taken from the LS, TL and ST planar sections, Fig. 1, and do not involve conversion factors. These particular sections were chosen because they are commonly used in microstructural characterization of the engineering alloys. To accurately and completely characterize the second phase dispersions, it is necessary to transform their two-dimensional (2-D) measurements to the three-dimensional (3-D) size and spatial distributions. There have been many attempts to develop stereological techniques for estimating the 3-D particle size distributions from the 2-D probes. The earliest work can be traced back to 1925 [10] and new techniques are proposed each year. Underwood, in his classic monography [2], has summarized all pre-1970s methods. Among them the DeHoff's approach [11], published in 1962, allowed for obtaining the size distribution of cylindrical ellipsoids from the measurements made on random plane sections. Subsequently DeHoff and Bousquet [12] developed methodology for obtaining size distribution of triaxial ellipsoids from the distribution of their linear intercepts. However, the application of both methods is limited because they assume that all spheroids have the same shape. Other stereological models published before 1970 also assume identical particle shapes and are applicable only to the particles with the most basic shapes [2]. Since particles in the engineering materials are neither simple-shaped nor identical, the applications of the above models to that class of materials is limited.

In the 1980s, a number of stereological methods for obtaining 3-D distributions for arbitrary oriented particles with different shapes have been proposed [13-18]. The point-sampled intercept method (PSIM) is one of them [19-21]. Its advantage is that, according to Gundersen *et al.* [13], it does not require assumption about particle shapes. The basic formula used in PSIM is:

$$\bar{v}_v = \frac{\pi}{3} \bar{l}_0^3 \quad (1)$$

which relates  $\bar{v}_v$ , the volume-weighted average volume of the particles to  $\bar{l}_0$ , the point-sampled intercept length. Although Eq. (1) gives an unbiased estimate of the average particle volume, it is important to emphasize that  $\bar{v}_v$  is an unconventional volume weighted average rather than the number average,  $\bar{v}_n$ , commonly used.  $\bar{v}_v$  is calculated from expression:

$$\bar{v}_v = \frac{[\bar{v}^2]}{\bar{v}_n} = \frac{\sum_{i=1}^n v_i^2}{\sum_{i=1}^n v_i} \quad (2)$$

where  $\bar{v}_i$ 's are volumes of individual particles. The PSIM method requires no assumption about the particle shapes, but it does require, as pointed out by Gokhale and Vander Voort [20], that the structure is isotropic. Moreover, the method gives only the average value and not the distribution.

Sterio [14] proposed another technique for 3-D size distribution analysis. In his disector method a counting system consisting of two parallel planes separated by a known distance  $h$  is used. An unbiased estimate of the number of particles in the specimen can then be obtained by counting the number of particles whose transects are completely or partially inside the counting system. Combined with standard stereological relations the method

yields the mean particle sizes on the disector sections. Three dimensional size distribution can be estimated using the similar principle from the sets of serial sections. This estimation procedure is the most efficient when  $h$  is about a one-third to one-fourth of the mean particle height. The method supposedly gives better estimation of the size distribution than PSIM. However, the obvious disadvantage of this approach is that finding the particle size distribution is extremely work intensive. For small particles (in the order of a few  $\mu\text{m}$ ) and/or volume fractions less than 1%, the measurements are also very difficult. For example, to obtain a statistically meaningful value of the average pore size in the 7050 alloy, it requires, for conventional methods, to measure pores on about 200 fields. In the case of the disector method it would be necessary to double that number. In addition, obtaining required two parallel plane sections few  $\mu\text{m}$  apart is extremely difficult.

A very general method for estimating 3-D distributions of sizes and shapes of creep cavities from size measurements made on polished plane sections has been recently proposed by T. -S. Liu *et al.* [22]. The problem was cast in the form of a double integral equation whose solution yields the size distribution. In this method both the aspect ratios and the orientations of spheroids can be varied and the method reduces to the DeHoff's approach [11] for particles with identical shapes. However, the shapes of the particles can be either oblate or prolate but not both at the same time. For particles lacking rotational symmetry, such as the pores and constituent particles in the 7050 alloy, this technique is of little value. Karlsson and Sandstrom [23] proposed similar method for evaluating 3-D size distribution of inclusions based on measurements from 2-D sections. They assumed that inclusions are ellipsoidal with non-cylindrical symmetry. The main drawback of their approach are the assumptions that all inclusions have the same shape factors and that they are all aligned.

To fully characterize second phase morphology, the size measurements have to be supplemented with the characterizations of spatial distributions. The spatial distributions are usually classified as regular, random, clustered and random with clusters. The regular distribution of points on a plane is easy to recognize as the points are arranged in a distinct pattern. To characterize such distribution it is necessary to specify only the point density and to identify the polygon comprising the pattern. The random distributions of points can be adequately characterized by the particle area density and the parameters of the Poisson distribution describing interparticle spacings.

Clusters of particles are more difficult to describe. The advantages and disadvantages of the methods developed for this purpose have been recently reviewed by Vander Voort [24]. Among them the number density [25], nearest neighbor spacing [26-28], Voronoi (Dirichlet) tessellation [25, 29-32] and image amendment methods [33,24] are the most often used. In the number density approach, the number of particles per unit area,  $N_A$ , is counted in successive locations, or fields, on the specimen section. For each field, the mean  $N_A$  and its standard deviation are found. An increase in the standard deviation for a given field indicates a greater degree of clustering. It is recommended that for the best result the size of the field should be equal to the size of a cluster. In the image amendment method, all particles separated by a distance less than or equal to a chosen critical spacing are fused together. The number of fused aggregates represents then a measure of clustering. The area fraction of particles in each cluster and the size of the cluster can also be determined. The key assumption in this method is the critical interparticle spacing and the method accuracy increases with the increase of the test field size. In the nearest neighbor method, the ratio of the mean nearest-neighbor distances for the real and the equivalent random microstructures and the ratio of their variances are calculated. These ratios are then used to determine the particle spatial distribution type [26]. In the Voronoi tessellation method the distribution of the tessellation cell areas, and the cells' area



variances are used to identify the particle spatial arrangement. The last two methods are related because near-neighbors can be uniquely identify after constructing Voronoi tessellation. Both methods have been used in this study and will be discussed further in the sections to follow. We also note that there have been attempts to use 3-D tessellation to characterize particle spatial distribution. In this case the cells form space-filling assemble of irregular polyhydra and the algorithms for their computation are readily available [34-36]. The applications of those 3-D tessellation techniques to the characterization of the 3-D particle spatial distributions have been studied by Saxl [37], Stoyan [38], Serra [39] and Santalo [40].

The 7050-T7451 plate alloy is an ideal material to test predictive capability of all described above techniques. This alloy has been recently intensively studied with the focus on the improvement of its fatigue durability [41-43]. Results showed that although most of the mechanical properties of slightly different alloy variants are practically the same, there are differences in the fatigue cracks initiation sites in different variants and this translates into significant differences in the fatigue lives [44,45]. This suggests that there are microstructural differences between variants and that they are responsible for the differences in fatigue durability. In addition it is also expected that each alloy variant has different through-thickness microstructural gradients. In this work the differences in the 7050-T7451 plate alloys constituent particle and pore size and spatial distributions, which are most likely responsible for fatigue behavior, have been quantify using described above methodologies. First, the linear intercept method was used to measure the average pore and particle sizes and their size variations at different locations within the plates. All resulting 2-D size distributions were tested for conformity with the normal and lognormal distribution types. The 3-D size distributions were then obtained by finding a 3-D computer simulated model microstructure having the same 2-D characteristics as the true microstructures. Secondly, the particle and pore volume fractions were estimated by

measuring their area fractions on plane sections. Thirdly, the shapes and orientations of the particles and the pores were characterized using the methodology proposed earlier by the authors [1,5]. Finally, spatial distributions of both phases were identified and characterized using a new method based on the linear intercept scan of the tessellation cells.

## EXPERIMENTAL

The materials investigated in the study were two variants of the 7050-T7451 plate alloys designated as old pedigree ("high" porosity) and new pedigree ("low" porosity), both obtained from *Alcoa Laboratories*. The new alloy shows improved fatigue life as a result of the microstructural refinements obtained through proprietary modifications of the composition and processing conditions. Samples for metallographic examinations of both alloy variants were taken from the longitudinal (TL), transverse (ST) and short transverse (LS) planes, and at three locations, i.e. at the surface, quarter depth and the center of the as-received plates. The locations of all test planes are shown in Fig. 1.

The samples used in metallographic examinations were prepared by mechanical grinding to a surface finish of 600 grit using wet SiC paper, followed by polishing on a felt wheel with 1  $\mu\text{m}$  and then 0.25  $\mu\text{m}$  diamond pastes mixed with ethanol. This procedure provided a clean surface with little particle pull-outs. Measurements of the porosity and the constituent particles were made on as-polished specimens to avoid alteration of particle shapes and number-densities by etching. All measurements were made from optical photographs taken at magnification 900X. A few SEM micrographs were also taken and used in the study of the particle shapes.

The magnification 900X used in all measurements was chosen as a compromise between efficiency and accuracy. It allowed for detection of a total of 3908 constituent particles in

both studied alloys. This corresponds to a total scan area of 22.42 mm<sup>2</sup> and to 217 particles per each test plane shown in Fig. 1. The number of detected pores was 3261, which is approximately 181 per test plane. The total area searched for the pores was 44.45 mm<sup>2</sup>. This area is twice the area scanned for the constituent particles because of the pores' lower volume fractions.

All micrographs obtained from metallographic examinations were digitized and saved as computer graphics files for subsequently analysis using our custom-made image analysis program. The program analyzes the images using the linear intercept method and automatically calculates the average intercept lengths, shape and orientation indices and aspect ratios of all second phase features. It also finds size distributions using appropriate probability plot [46], constructs tessellation cell networks and analyzes particle spatial distributions.

To find second phase volume fractions it was assumed that they were equal to the area fractions. For each depth location the volume fraction was calculated as the average of the area fractions on TL, ST and LS planes. For each plane these fractions were calculated as the ratio of the number of pixels inside particles to the total number of pixels in the entire field. Alternatively, the volume fractions were also estimated using the point-sampled intercept length method [19-21]. In this method, the volume fraction is assumed equal to the ratio of the random sampling points hitting the particles to the total number of sampling points. However, the results obtained using point-sampled method changed slightly with the number of sampling points, therefore this method was abandoned.

#### **A. Two-Dimensional Size Distributions**

The sizes of the pores and particles on the plane sections were measured using the linear intercept method. In this method the average intercept length,  $L_2(\alpha)$ , of a two dimensional object at a scan angle  $\alpha$  can be calculated as [47]

$$L_2(\alpha) = \frac{A}{H_2(\alpha)} \quad (3)$$

where  $A$  is the object area and  $H_2(\alpha)$  is the tangent height defined as the projection of the measured object on the direction perpendicular to the scan lines. The average intercept length over all scan angles,  $L_{II}$ , is defined in this case as:

$$L_{II} = \frac{1}{\pi} \int_0^\pi w_2(\alpha) L_2(\alpha) d\alpha \quad (4)$$

where  $w_2(\alpha)$  is the weight factor equal to:

$$w_2(\alpha) = \frac{H_2(\alpha)}{\frac{1}{\pi} \int_0^\pi H_2(\alpha) d\alpha} \quad (5)$$

For convex shapes,  $\int_0^\pi H(\alpha) d\alpha$  is equal to  $L_p$ , the perimeter of the measured object. Thus in this case

$$L_{II} = \frac{\pi A}{L_p} \quad (6)$$

which is a standard equation used in the literature [47]. To study the directional variation of the average intercept length, we also define a normalized intercept length,  $d(\alpha)$ , as

$$d(\alpha) = d = \frac{L_2(\alpha)}{L_{2,max}} \quad (7)$$

where  $L_{2,max}$  is the maximum average intercept length. The  $d$  vs.  $\alpha$  plot can be subsequently used to compare object shapes [5].

To compare differences between the pore and particle sizes of the new and the old pedigrees 7050 alloys the standard one factor ANOVA (analysis of variance) has been performed. In this analysis, the actual  $F$  value is compared with the critical  $F$  value for 5%

significance level. If the actual F value is smaller than the critical one, then the null hypothesis that the pore or particle sizes in both alloys have the same mean could not be rejected. This means that the average pore or particle sizes of the two pedigrees are statistically the same at 95% probability.

### **B. Three-Dimensional Size Distributions**

The transformation of 2-D measurements to the 3-D size distributions has been carried out assuming that all second phase features are ellipsoids with different sizes but identical aspect ratios. To find their size distributions a numerical approach was used. A computer program developed for this purpose generated a model microstructure consisting of a 3-D spatial distribution of ellipsoids with the same aspect ratios but different sizes. Then the program sectioned the model microstructure along TL, LS and ST planes, estimated the intercept lengths for each plane and compared results with those obtained for 7050 alloy. When the differences between the means and standard deviations of the 2-D size distributions for the model and for the studied alloy were minimum, then the ellipsoids in the model were assumed to be the best approximation to the particles in the real alloy. The measurement of the goodness of fit,  $R_e$ , used by the program had the following form:

$$R_e = \frac{1}{6} \sqrt{\sum_{i=1}^3 \left( \left( \frac{\Delta\mu_{LII,i}}{\mu_{LII,exp,i}} \right)^2 + \left( \frac{\Delta\sigma_{LII,i}}{\sigma_{LII,exp,i}} \right)^2 \right)} \quad (8)$$

where  $\Delta\mu_{LII}$  and  $\Delta\sigma_{LII}$  are the differences between means and standard deviations of  $L_{II}$  for the experimental and simulated microstructures and  $\mu_{LII,exp,i}$  and  $\sigma_{LII,exp,i}$  are the values of mean and standard deviation obtained experimentally. The data for ST, LS and TL planes correspond to  $i = 1, 2$  and  $3$  respectively. The definition of  $R_e$  is not unique and other

forms including for instance weight functions added to both terms in Eq. (8) could also be used.

The input variables to the 3-D model were (1) ellipsoids size distribution parameters, (2) their alignment, and (3) their spatial distributions. The radii of ellipsoids were designated as  $a$ ,  $b$  and  $c$  respectively with  $a$  being the largest. The ratios  $a/b$  and  $a/c$  served as input parameters and they could vary from 1 to  $\infty$  to accommodate shapes from a sphere ( $a = b = c$ ) to an arbitrary ellipsoid. The size of each ellipsoid was characterized by its largest radius,  $a$ , and it was assumed that those sizes obeyed either normal or lognormal distribution. The maximum radius of each ellipsoid,  $a$  or  $a[i]$ , was obtained from the normal standard variable,  $Z$ , and the assumed mean,  $\mu_a$ , and standard deviation,  $\sigma_a$ , using expression:

$$a[i] = \mu_a + Z[i]\sigma_a \quad (9)$$

In case of the lognormal distribution, all size dimensions were converted into their logarithmic values.  $Z[i]$  was calculated using the method by D'Agostino [48] described in the Appendix.

To generate a random dispersion of ellipsoids in a given volume, the coordinates of the center of each ellipsoid,  $(x, y, z)$ , were independently and randomly selected within the dimension of a given volume. Each location was then checked to assure no overlapping between ellipsoids. If overlapping took place the location was rejected and a new random location generated again. As a result the spatial distribution of the ellipsoids was not exactly random but pseudo-random or non-intersecting random. The orientation of each ellipsoid was defined by three Euler angles which were also independently and randomly generated. The orientations of ellipsoids in the model could be varied from totally oriented to random. The orientation distribution was assumed to be known a priori, and treated as an input variable in the program. The spatial randomness of the simulated

microstructures was tested by examining a collection of 1,000 identical spheres. The theoretical average intercept length  $L_3$  is in this case [2]:

$$L_3 = \frac{4V}{S} = \frac{4r}{3} \quad (10)$$

where  $V$ ,  $S$  and  $r$  are the volume, surface area and radius of the sphere respectively. The value of  $L_3$  obtained for the simulated microstructure had relative error of only 2.9%.

### C. Shapes and Alignment

To quantify shapes of second phase features the shape index,  $SI$ , equal to the area under the  $d$  vs.  $\alpha$  curve has been used [1]. This index can be expressed as

$$SI = \frac{1}{\alpha_p} \int_0^{\alpha_p} \frac{L_2(\alpha)}{L_{2,\max}} d\alpha = \frac{1}{\alpha_p} \int_0^{\alpha_p} d d\alpha \quad (11)$$

where  $\alpha_p$  is the angular period of the  $d$ - $\alpha$  curve. As demonstrated elsewhere [5],  $SI$  is independent of the measured object size and orientation. It has values between zero and one, and can be viewed as an indication of how circular is the object. For a perfect circle the shape index,  $SI$ , is equal to one and its values for typical two-dimensional shapes can be found in Ref. [5].

For a group of objects, two different normalized lengths, the *average*  $d$  and the *global*  $d$  [1,5] can be used. The global  $d$ - $\alpha$  curve obtained using standard intercept length measurements, shows the change of the object normalized intercept length with directions. The average  $d$ - $\alpha$  plot, obtained by 'aligning' all the objects before scanning, represents the pure object shapes as the orientation effect is eliminated. To illustrate the difference let's

assume that two identical elongated particles are rotated with respect to each other. Their individual  $d$ - $\alpha$  curves will have a phase difference and the average, represented by the global  $d$ - $\alpha$  curve, will reflect both the shapes and the orientations of both particles. Consequently the global shape index,  $SI_g$ , which is the area under the global  $d$ - $\alpha$  curve, represents true particle shapes only if the particles are aligned. Since in general they are not,  $SI_g$  increases with increasing particle misalignment and approaches unity for a statistically random structure. The "true" average shape index for all particles can be obtained by constructing the average  $d$ - $\alpha$  curve for particles artificially aligned along axes corresponding to  $L_{2,max}$ . We shall call the shape index resulting from such curve  $SI_{avg}$ . Since  $SI_{avg}$  does not contain the information about particle orientation, comparing it with  $SI_g$  allows for the deconvolution of the shape and orientation components. This is done through an orientation factor,  $\Omega$ , defined as:

$$\Omega = \frac{1 - SI_g}{1 - SI_{avg}} \quad (12)$$

For randomly oriented features,  $SI_g$  is equal one and  $\Omega$  will be zero. For a perfectly oriented structure  $SI_g$  is equal to  $SI_{avg}$  and  $\Omega$  is one. The orientation factor,  $\Omega$ , allows thus to quantify, on a scale from zero to one, the degree of particle orientation. This factor is used to describe particle orientation distribution in our 3-D simulation program.

Another parameter commonly used to describe the degree of alignment is the ratio of the total length of oriented lines in the microstructure to the total length of all lines,  $\Omega_{1,2}$ . This ratio was introduced by Saltykov[6] and in our case it is equal to [1]:

$$\Omega_{1,2} = \frac{L_2(\alpha=0) - L_2(\alpha=90)}{L_2(\alpha=0) + 0.571 L_2(\alpha=90)} \quad (13)$$



$\Omega_{1,2}$  is zero for a random structure and approaches one for structure with highly oriented and elongated particles. However, it is not guaranteed that the structure is random when  $\Omega_{1,2}$  is zero because eq. (13) is strictly valid only for partially oriented lines. Therefore, we prefer to use  $\Omega$  in Eq. (12), which uses the average values over all the scan angles as a more precise measure of particle alignment.

#### **D. Spatial Distributions**

The spatial distributions of the second phase particles have been studied with the help of the Voronoi tessellation constructions[25-32]. Two dimensional Voronoi cells are plane-filling polygons with the sides of each polygon constructed as the bisectors of the lines connecting centers of the neighboring particles. This way each polygon contains one second phase particle and the ratio of the polygon area to its particle area is defined as the "local area fraction". With the help of tessellations the spatial distribution of particles can be analyzed by studying the particle local area fractions, average cell areas and their standard deviation and/or average numbers of cell sides and their standard deviation, etc. [25-32]. However, the obtained results are approximations as ideally three dimensional Voronoi tessellations should be used for spatial characterizations. Another method for classifying the spatial distribution of the second phase particles is the nearest neighbor spacing method [26] which utilizes two indexes, Q and R, defined as follows:

$$Q = \frac{\text{Observed Nearest Neighbor Distance}}{\text{Expected Nearest Neighbor Distance}} \quad (14)$$

$$R = \frac{\text{Observed Nearest Neighbor Distance Standard Deviation}}{\text{Expected Nearest Neighbor Distance Standard Deviation}} \quad (15)$$

where the expected values are calculated by assuming a random structure with the same point density as the experimental one. Note the above definition of  $R$  is based on the standard deviations instead of the variances as originally proposed by Schwartz and Exner [26]. However, the two definitions converge to the same exact critical values,  $R = 1$ , under the same conditions. To identify different types of spatial distribution the following guidelines can be used: (1) for the clustered distribution,  $Q < 1$  and  $R < 1$ ; (2) for regular distribution  $Q > 1$  and  $R > 1$ ; (3) for random distribution with clusters  $Q < 1$  and  $R > 1$ , and (4) for totally random distribution  $Q = 1$  and  $R = 1$ .

In addition to using  $Q$  and  $R$  to identify spatial distribution patterns, a tessellation cell shape method has been tried. In this method, the sizes and shapes of the tessellation cells are analyzed using the same methods as those for the second phase dispersions. The advantage of this approach, originally suggested by Wary et al. [27], is that it allows for the detection of the fluctuations in the cell orientations. By using this technique, all methodologies developed for characterizing 2-D objects can be applied to characterize the polygonal tessellation cells. Consequently for a totally random set of points representing second phase centers, the resulted Voronoi tessellation cells should also be randomly oriented and their shape index,  $SI$ , should be equal to one. If the point distribution is regular, for example rectangular or hexagonal, the shape indexes are smaller than one and their values are also known [5]. The  $d-\alpha$  curves for the tessellation cells constructed on particles or pores can be thus compared with those for the random and/or the regular patterns to identify their spatial distribution type. Since most results published so far correlate the cell area distributions to the point distributions [29, 32], one can use tessellation cell shape method to gain additional information on the particle spatial distribution. The tessellation cell shape method is particularly useful for analyzing the orientations of the second phase clusters which cannot be detected by the other two spatial distribution methods. This is because in an ideal clustered structure any location and/or

orientation changes of a whole cluster will not affect the values of Q and R because the nearest neighbor spacing remains the same. The tessellation cell shapes, on the other hand, are sensitive to any anisotropy in the cluster orientations spacings and cells d- $\alpha$  curves and  $SI_g$ 's indexes can be used to analyze those inhomogeneities. As a result the information on the spatial distributions provided by the cell shape method and the Q-R index method are complementary: the former gives information about orientation isotropy and the latter characterizes the spatial distribution type. All above methods have been used to analyze pore and the constituent particle patterns in this work.

## RESULTS AND DISCUSSIONS

### A. Pores

#### 1. Volume fraction

The average pore volume fractions, the number of detected pores and the number of fields used in the measurements are listed for each test plane in Table 1. As already explained, the volume fractions were assumed equal to area fractions and their average values were 0.135% for the old and 0.103% for the new pedigree alloys. The porosity level in the new 7050 alloy has been thus reduced by 24%. The through-thickness porosity volume fraction gradients are shown in Figure 2, with each data point representing the average for TL, LS and ST planes at a given plate location. As expected, the average pore volume fractions are the highest at the center and the lowest near the surface for both studied plates. However, the porosity levels are practically the same for both pedigrees at the surface and quarter-depth locations but are higher at the center regions for the old alloy. The reduction of the average porosity level in the new alloy comes then mainly from the center region.

## 2. Size, shape and alignment

A typical pore and shapes of 201 pores found on the ST plane at the center of the old plate are shown in Figs. 3 and 4 respectively. The results of quantitative characterizations of these and all other pore sizes, shapes and alignments are summarized in Table 1. The average pore sizes are represented in Table 1 by the average intercept length,  $L_{II}$ , measured at scan angles from 0 to 180° in increments of 5°. To show the change of pore intercept lengths with directions the  $L_{\gamma}$ - $\alpha$  curves have been used, Figs. 5 and 6. These curves are ellipsoidal and they represent particle profiles on different plane sections in 3-D space. The information provided by  $L_{II}$  and  $L_{\gamma}$ - $\alpha$  plots are complimentary.  $L_{II}$  represents the overall average pore size changes while  $L_{\gamma}$ - $\alpha$  plots show the variation of the pore sizes with orientation and location within the plate. The average values of  $L_{II}$  were 3.39  $\mu\text{m}$  for the old and 3.47  $\mu\text{m}$  for the new alloy. The through-thickness gradients of  $L_{II}$  are shown in Figure 7. For the old 7050 variant, the average pore size is the smallest near the plate surface and increases toward the plate center. For the new pedigree, the smallest pore size is also near the plate surface but there is almost no size change between quarter-depth and the center. Considering the variation of pore volume fractions, Fig. 1, it appears that both studied alloys have strong microstructural gradients and the plate centers has the largest pores.

Cumulative 2-D pore size distributions for both investigated alloys have been compiled in Figure 8. The pore size measure used in the figure is as before  $L_{II}$ , the average intercept length. The plots in Fig. 8 show both the size ranges and the differences between the pore sizes at different locations for each pedigree. Comparison of the distributions suggests that the pores in the new alloy are not only smaller but also have narrower distribution than those in the old one. To further quantify the size distributions they were fitted with both the normal and the lognormal distributions, using appropriate probability plots[46] and employing the correlation coefficient,  $R^2$ , to measure the goodness of fit. In all cases

the pore sizes followed the lognormal distribution with  $R^2$  close to one. The obtained distribution parameters are listed in Table 2 and an example of a typical size frequency distribution and the lognormal fit are shown in Figs. 9 and 10.

The 3-D pore size distributions were estimated using described earlier numerical method and assuming that pores could be represented by triaxial ellipsoids. The results are presented in Figure 11 together with the original experimental data. The 3-D size measures used in Fig. 11 are the maximum intercept lengths,  $L_{//,max}$ , in the plane containing ellipsoid center and the major axes. As in the case of the 2-D size distribution, the lognormal distribution gives a better match between the simulated and experimental results than the normal one. The means, standard deviations and aspect ratios of the 3-D lognormal size distributions for both alloys are listed in Table 3. As expected, Fig. 11, the maximum average intercept lengths of the 3-D ellipsoids are larger than the 2-D experimental results. This is because for a given ellipsoid any 2-D intercept length is always smaller than or equal to its 3-D  $L_{//,max}$ . Consequently the experimental 2-D data should approach the 3-D values for larger pore sizes as it is indeed the case in Fig. 11. The goodness of fit of the estimated 3-D size distribution was evaluated using the value of the normalized errors,  $R_e$ , which are also listed in Table 3. Alternatively, the error can be evaluated by comparing the 2-D experimental size distributions with their equivalents for the simulated microstructure. An example of such comparison is shown in Figure 12 where the two resulting curves are very close over the entire size range. The fits could be further improved if other distributions, for example Gumbel or three parameter lognormal and/or different aspect ratios for ellipsoids were used. Work on the implementation of these improvements is in progress. We also realize that the format of the normalized error  $R_e$  is not unique and that the results will be different for differently defined  $R_e$ 's. Despite these limitations, the obtained approximations of the 3-D pore sizes have sufficient accuracy for use in the mechanical behavior models.

To compare the pore sizes,  $L_p$ , in the new and the old 7050 alloys the one factor ANOVA has been performed. The experimental  $F$ -value is in this case equal to 3.177 and it is smaller than the critical  $F$ -value of 3.844 for the 5% confidence level. Consequently, the null hypothesis that the pore sizes for both pedigrees have the same mean could not be rejected, and the average pore sizes of the two pedigrees are statistically the same at 95% probability. However, the tails of the size distributions are very different, especially at the larger size regime. For example, there are 23 pores in the old pedigree with diameters larger than 10  $\mu\text{m}$  but only 9 for the new pedigree. Since only the largest pores act as the fatigue crack initiation sites, it is the upper tail of the size distribution, not the average value, that controls the fatigue behavior. This illustrates the importance of the complete quantitative microstructural analysis.

The pore shapes have been characterized using the  $d$ - $\alpha$  plots [1, 5], Figs. 13 and 14. Fig. 13 shows the global  $d$  and the average  $d$  curves in rectangular coordinates. Fig. 14 shows the change of average  $d$  on polar plot. Note that Fig. 14 represents the average outline profile of the pores. The shape index,  $SI$ , calculated from  $d$ - $\alpha$  plots in Fig. 13 for the pores in the center region, ST plane of the old alloy, was 0.82. The average shape indexes for pores on all test planes were 0.816 and 0.831 for the new and old alloys respectively. This means that the average shape of the pores on 2-D sections is ellipsoidal with the average ratios of the shortest to the longest axes of 0.816 and 0.831 for new and old alloys respectively. The corresponding average pore aspect ratios defined as the ratios of the average  $d$  at 0 to 90°, were 1.45 and 1.51. Since the pores were irregular, the shape index  $SI$ , which contains information from all the scan angles, was a better descriptor of the shapes than the aspect ratio. However, the results from both methods suggest that the pore morphology in both studied alloys were similar as the relative difference between  $SI$ 's was less than 2% and for the aspect ratios it was only 4%. The change of pore shapes with location within the plate is shown in Figure 15. It is evident that the changes are

small and that the pores in the old alloy are slightly more elongated than their counterparts in the new alloy. We attribute these differences to different thermo-mechanical treatments.

The orientation factors,  $\Omega$ , for the pores on different sections are listed in Table 1. They vary from 0.11, which corresponds to almost random structure, to 0.65 which indicates partial alignment. The average values are 0.38 for the new and 0.32 for the old pedigrees. Since  $\Omega$  in Eq. (12) increases as the pores become more and more circular and/or more randomly oriented, the alignment of pores in the studied alloys can be considered as insignificant. The change of the average  $\Omega$  values, for ST, TL and LS planes with location are shown in Figure 16. Results suggest slightly larger degree of alignment, particularly at the surface region, in the new alloy. These average  $\Omega$  values were used as input data in the numerical estimation of the true ellipsoid sizes.

The results of the characterizations of the pore shapes and orientations provide important information to the fatigue life prediction models. Since the largest pores act as the fatigue crack initiation sites, their shapes and sizes determine the maximum dimension of the 'initial flaw'. The alignment factor,  $\Omega$ , offers additional information on the relative orientation of the pore axis with respect to the axis of the applied stress. Both of them are important factors controlling fatigue lives.

## **B. Constituent Particles**

### **1. Volume fraction**

The 7050-7451 plate alloy contains two different types of particles:  $\text{Al}_7\text{Cu}_2\text{Fe}$  and  $\text{Mg}_2\text{Si}$ . Since both types were found at the fatigue crack initiation sites they were characterized without distinction to their chemical compositions using the same methods as for pores.

The average particle volume fractions, the number of measured particles and the number of viewing fields used in the measurements are listed in Table 4. The obtained constituent particle area fractions were 0.61% for the new and 0.70% for the old alloy. This difference is the most significant improvement in the new 7050-T451 plate alloys which came out from our microstructural analysis. The through-thickness particle volume fraction gradients have been plotted in Fig. 2. They indicate that new pedigree contains fewer particles at both center and quarter depths than the old one but the opposite is true at the surface. Despite that the new alloy has, on average, fewer particles than the old one.

## 2. Size, shape and alignment

A typical collection of constituent particles found on the ST plane at the center of the plate in the old alloy is shown in Fig. 17. The average 2-D sizes for constituents, measured on all nine sections, were  $4.02\text{ }\mu\text{m}$  for the new pedigree and  $4.77\text{ }\mu\text{m}$  for the old alloy, Table 4. The average "size profiles" of the constituent particles are shown in Figs. 18 and 19. The apparent particle sizes are always the smallest on the ST planes due to the elongated particle shapes resulting from rolling. The null hypothesis that the particle sizes for the new and old alloy were the same had to be rejected since the resulting experimental *F*-value, 34.272, is much larger than the critical *F*-value of 3.844 for 5% significance level. Therefore the average particle size in the old alloy is, at 95% probability level, larger than that in the new one. The change of particle sizes with depth for both alloys is shown in Fig. 7. The size increases toward the plate center and, for example, the average sizes for the new alloy are 3.25, 3.87 and  $4.93\text{ }\mu\text{m}$  at the surface, quarter depth and the center of the plate respectively. The differences are most likely due to the temperature variation during the thermal-mechanical processing. The cumulative particle 2-D size distributions, typical size frequency distribution and the lognormal fit are shown in Figs. 20, 21 and 22 respectively. As for the pores, the particle sizes also have lognormal distribution with  $R^2$



close to one. The parameters of the obtained lognormal fit are listed in Table 5 and characteristics of the calculated true 3-D size distribution are summarized in Table 3.

The  $d$ - $\alpha$  plots for constituent particles are shown in Fig. 23 and 24. Their analysis revealed that particles in the old alloy had average shape index  $SI$  equal 0.74 and aspect ratio of 1.86. For the new alloy these values were 0.68 and 2.28 respectively, Table 4. This means that the constituents are elongated, ellipsoidal in shape and aligned with the rolling direction[1]. However, we have also observed instances of isolated, round and slightly oval constituent particles as well. The through-thickness shape index variations are shown in Fig. 15. They suggest that particles in the old alloy are more circular particularly at quarter depth and surface regions. The average  $\Omega$  values for the constituent particles, Table 4, are 0.52 and 0.43 for the new and old alloys respectively indicating a moderate alignment. The change of  $\Omega$  from the surface to the center of the plate is shown in Fig. 16. The results show that the alignment exists only at the surface and center regions of the plates. Comparing characteristics of the pores and the particles in both alloys it appears that the particles have higher volume fraction and larger sizes and that they are more elongated and aligned than pores.

### **C. Spacing and Clustering of Pores and Particles**

The particle and pore spatial distributions have been quantified using the tessellation method. Figure 25 shows an example of the Voronoi tessellation cell construction for the pores on the ST plane at the center location of the old alloy. Table 6 lists some of the characteristics obtained from the analysis. The most important among them are local volume fractions and near and nearest neighbor distances -- these quantities can be obtained unambiguously only from the tessellations. The observed nearest neighbor distance in this case was 48.2  $\mu\text{m}$  with standard deviation of 33.2  $\mu\text{m}$ . The expected

counterparts for the random structure with the same point density are 51.86 and 27.18  $\mu\text{m}$  respectively. This gives  $Q = 0.929$  and  $R = 1.224$  which suggests that the distribution of the pores can be classified as random with clusters. For the constituent particles at the same location the observed nearest neighbor distance was 25.2  $\mu\text{m}$  with standard deviation 19.2  $\mu\text{m}$  while expected values are 27.64 and 14.45  $\mu\text{m}$  respectively. This gives  $Q = 0.879$  and  $R = 1.281$  which again suggests that the distribution is random with clusters. Above information about the second phase spatial distributions on all sections at the centers of the plates have been compiled in Table 7. In all cases the spatial distributions are random with clusters. It is also possible to carry the spatial characterizations further by considering the second phase cluster density, the number of the features per cluster, the cluster size, etc. and we are currently working on the implementation of methodologies allowing for such characteristics. We again emphasize that ideally one should use 3-D tessellations to study the spatial distribution. As pointed out earlier, the main difficulty in this case is acquisition of the data on the 3-D particle locations, which makes the method impractical.

An example of the results obtained from the shape analysis of the tessellation cells is shown in Fig. 26. The cells analyzed are those from Fig. 25 and the method used is the same as the one utilized for characterizing shapes of pores and particles. Fig. 26 shows the  $d-\alpha$  curve obtained for the cells and, for comparison, the curves for the random and rectangular point patterns. The  $SI_g$  for the tessellation is 0.963 while it is 1 for the random and 0.760 for the rectangle patterns. The shape index,  $SI_{avg}$ , is in this case equal to 0.736 which gives orientation factor  $\Omega$  of 0.138. The average cell aspect ratio is 1.872. As discussed earlier, a high value of  $SI_g$  combined with a low value of  $\Omega$  indicates near isotropic cell structure. The values of aspect ratio and  $SI_{avg}$  suggest that individual cells are in this case elongated and ellipsoidal. Work on the refined version on the cluster characterization methodology is in progress.

## CONCLUSIONS

- The volume fractions, sizes, shapes and orientations of pores and constituent particles in two different variants of 7050-T7451 Al plate alloy have been quantified. The characterizations included measurements of not only the average values of all microstructural descriptors, but also their distributions for TL, ST and LS planes at the surface, quarter depth and at the center of each plate.
- The lognormal distribution has been found to give the best description of the size distribution for both pores and particles. The average pore sizes were statistically the same in both studied alloys but the average particle size in the old alloy is larger than that in the new one. The new alloy has improved microstructures which contains 24% less pores and has smaller particles than the old one.
- In both alloys the pores are elongated with the average aspect ratio of 1.50. For constituent particles the average aspect ratio is 2.0. The spatial distributions of both pores and particles were characterized using the nearest neighbor spacing and the Voronoi tessellation methods. In all cases they can be classified as random with clusters.
- A numerical method for estimating the 3-D size distributions from the experimental 2-D measurements made on plane sections has been developed. The method assumes that particle sizes and shapes can be modeled as collection of triaxial ellipsoids with random, partially aligned or totally aligned orientations. The method has been used to obtain 3-D size distributions of pores and constituent particles in the 7050-T7451 Al plate alloy.

- The shapes of tessellation cells, built on particle or pore centers, have been analyzed to quantify the second phase spatial distributions. The results have been compared with those for random and various regular point sets to provide additional information about the pore and particle spatial distribution patterns.

#### **ACKNOWLEDGMENTS**

The authors would like to thank the Office of Naval Research for their support under Grant No. N00014-91-J-1299 of which Dr. A. K. Vasudevan is the program manager.

Thanks are also due to Drs. R. J. Bucci, A. J. Hinkle and P. E. Magnusen from Alcoa Laboratories for providing the material used in this study and for valuable discussions.

## APPENDIX

The standard random variable,  $Z$ , can be approximated as[46]

$$Z = \text{sign}[F_N(x) - 0.5][1.238t(1 + 0.0262t)] \quad (\text{A1})$$

where

$$t = \sqrt{-\ln[4F_N(x)(1 - F_N(x))]} \quad (\text{A2})$$

$$\text{sign}(F_N(x) - 0.5) = \begin{cases} +1, & F_N(x) - 0.5 > 0 \\ -1, & F_N(x) - 0.5 < 0 \end{cases} \quad (\text{A3})$$

$$F_N(x_i) = \frac{i - 0.5}{N} \quad (\text{A4})$$

where  $N$  is the sample size and  $i$  is the observation number. To obtain probability plots one needs to plot the standard variable  $Z$  has been plotted as a function of a random variable  $x_i$  for the normal or  $\ln(x_i)$  for the lognormal distributions.

## REFERENCES

1. J. Zhang, A. J. Luévano and M. A. Przystupa, "Quantitative Analysis of Heterogeneous Structures of Aluminum 7050 Alloy", *Scripta Metallurgia et Materialia*, 26, pp. 1061-66, (1992).
2. E. E. Underwood, *Quantitative Stereology*, Addison-Wesley Publishing Company, Reading, Massachusetts, pp.196-197, (1970).
3. R. T. DeHoff and F. N. Rhines, editors, *Quantitative Microscopy*, McGraw-Hill Book Company, New York, NY 10036, USA (1968).
4. G. F. Vander Voort, *Metallography Principles and Practice*, McGraw-Hill Book Company, New York, NY 10036, USA (1984).
5. J. Zhang, A. J. Luévano and M. A. Przystupa, "Microstructural Models for Quantitative Analysis of Grain and Particle Shapes", to be published in *Materials Characterization*, (1994).
6. J. E. Hilliard, "Specification and Measurement of Microstructural Anisotropy", *Trans. Met. Soc. AIME*, 224, pp. 1201-1207, (1962).
7. T. Reti and I. Czinege, "Shape Characterization of Particles via Generalized Fourier Analysis", *J. of Microscopy*, 156, Pt. 1, pp. 15-32, (1989).
8. J. L. Chermant, M. Coster and G. Gougeon, "Shape Analysis in  $R^2$  Space Using Mathematical Morphology", *J. of Microscopy*, 145, Pt. 2, pp. 143-157, (1987).
9. S. A. Saltykov, *Stereometric Metallography*, Second Edition, Moscow, Metallurgizdat, (1958).
10. S. D. Wicksell, "The corpuscle problem. A mathematical study of a diametric problem," *Biometrika*, vol. 17, pp. 84-99, 1925.
11. R. T. DeHoff, "The determination of the size distribution of ellipsoidal particles from measurements made on random plane sections," *Transactions of The Metallurgical Society of AIME*, vol. 224, pp. 474-477, June 1962.
12. R. T. DeHoff and P. Bousquet, "Estimation of the size distribution of triaxial ellipsoidal particles from the distribution of linear intercepts," *J. of Microscopy*, vol. 92, pt. 2, October 1970, pp. 119-135.
13. H. J. G. Gundersen and E. B. Jensen, "Particle sizes and their distributions estimated from line- and point sampled intercepts. Including graphical unfolding," *J. of Microscopy*, vol. 131, pt. 3, September 1983, pp. 291-310.
14. D. C. Sterio, "The unbiased estimation of number and sizes of arbitrary particles using the disector," *J. of Microscopy*, vol. 134, pt. 2, May 1984, pp. 127-136.
15. E. B. Jensen and H. J. G. Gundersen, "The stereological estimation of moments of particle volume," *J. Appl. Prob.* vol. 22, pp. 82-98, 1985.

16. H. J. G. Gundersen, "Stereology of arbitrary particles," *J. of Microscopy*, vol. 143, pt. 1, July 1986, pp. 3-45.
17. L. M. Cruz-Orive, "Particle number can be estimated using a disector of unknown thickness: the selector," *J. of Microscopy*, vol. 145, pt. 2, February 1987, pp. 121-142.
18. H. J. G. Gundersen and E. B. Jensen, "Stereological estimation of the volume-weighted mean volume of arbitrary particles observed on random sections," *J. of Microscopy*, vol. 138, pt. 2, May 1985, pp. 127-142.
19. S. Srinivasan, J. C. Russ and R. O. Scattergood, "Grain size measurements using the point-sampled intercept technique," *Scripta METALLURGICA et MATERIALIA*, vol. 25, pp. 931-934, 1991.
20. G. F. Vander Voort and A. M. Gokhale, "Comments on 'Grain size measurements using the point-sampled intercept technique'," *Scripta METALLURGICA et MATERIALIA*, vol. 26, pp. 1655-1660, 1992.
21. S. Srinivasan, J. C. Russ and R. O. Scattergood, "Reply to Comments on Grain size measurements using the point-sampled intercept technique by G.F. Vander Voort and A. M. Gokhale," *Scripta METALLURGICA et MATERIALIA*, vol. 25, pp. 1661-1662, 1992.
22. T. -S. Liu, D. G. Harlow, and T. J. Delph, "Stereological analysis of creep cavities on polished sections", *Metallography*, 21. pp. 55-76 (1988).
23. L. Karlsson and R. Sandstrom, "Evaluation of three-dimensional size distributions of inclusions," *Metallography*, vol. 19, pp. 143-176, 1986.
24. G. F. Vander Voort, "Computer-aided microstructural analysis of specialty steels", *Materials Characterization*, 27, pp. 241-260, (1991).
25. M. T. Shehata and J. D. Boyd, "Measurement of spatial distribution of inclusions", *Inclusions and Their Influence on Material Behavior*, R. Rungta ed. ASM International, Metals Park, OH, pp. 123-131, (1988).
26. H. Schwarz and H. E. Exner, "The Characterization of the Arrangement of Feature Centroids in Planes and Volumes", *J. Microscopy*, pp.129-55, (1983).
27. P. J. Wray, O. Richmond, H. L. Morrison, "Use of the Dirichlet Tessellation for Characterizing and Modeling Nonregular Dispersions of Second-Phase Particles", *Metallography*, 16, pp. 39-58, (1983).
28. W. A. Spitzig, J. F. Kelly and O. Richmond, "Quantitative Characterization of Second-Phase Population", *Metallography*, 18, pp. 235-261, (1985).
29. H. Hermann, H. Wendrock and D. Stoyan, "Cell-Area Distributions of Planar Voronoi Mosaics", *Metallography*, 23, pp.189-200, (1989).
30. T. N. Ronus, J. M. Fridy, K. B. Lippert and O. Richmond, "Quantitative characterization and modeling of second phase populations through the use of

- tessellations", *Simulation and Theory of Evolving Microstructures*, M. P. Anderson and A. D. Rollett eds. The Mineral, Metals & Materials Society, pp. 269-275, (1990).
31. J. R. Brockenbrough, W. H. Hunt Jr. and O. Richmond, "A reinforced material model using actual microstructural geometry", *Scripta Metallurgia et Materialia*, 27, pp. 385-390, (1992).
  32. R. K. Everett, "Analysis and modeling of fiber clustering in composites using N-tuples", *Scripta Metallurgia et Materialia*, 28, pp. 663-668, (1993).
  33. W. B. James, "Use of image analysis for assessing the inclusion content of low-alloy steel powders for forging applications", *Practical Applications of Quantitative Metallography*, ASTM STP 839, J. L. McCall and J. H. Steele, Jr., eds., American Society for Testing and Materials, Philadelphia, pp. 132-145, (1984).
  34. A. Bowyer, "", *The Computer J.*, 24, 2, pp. 162, (1981).
  35. D. F. Watson, *The Computer J.*, 24, 2, pp. 167, (1981).
  36. C. L. Lawson, *Computer Aided Geometric Design* 3, pp. 231, (1986).
  37. I. Saxl, "Contact distances and random free paths," *J. Microscopy*, 170, Pt. 1, pp. 53-64, (1993).
  38. D. Stoyan, W. S. Kendall and J. Mecke, *Stochastic Geometry and its Applications*. Akademie Verlag, Berlin. (1987)
  39. J. Serra, *Image Analysis and Mathematical Morphology*. Academic Press. London. (1982).
  40. L. A. Santalo, *Integral Geometry and Geometrical Probability*. Addison-Wesley, Reading, Mass. (1976).
  41. P. E. Magnusen, A. J. Hinkle, R. J. Bucci, R. L. Rolf and D. A. Lukasak, "Methodology for the Assessment of Material Quality Effects on Airframe Fatigue Durability," *Fatigue 90*, Honolulu, HA July 15-20.
  42. P. E. Magnusen, A. J. Hinkle, W. Kaiser, R. J. Bucci and R. L. Rolf, "J. of Testing and Evaluation", November 1990, pp. 439-445.
  43. P. E. Magnusen, R. J. Bucci, A. J. Hinkle, M. E. Artley and R. L. Rolf, "The influence of Material Quality on Airframe Structural Durability," *Advances in Fracture Research*, 2, edited by Salama et al. pp. 999-1006, (1989).
  44. M. A. Przystupa, J. Zhang and A. J. Luévano, "Development of the microstructure based stochastic life prediction models," Program Report, ONR Grant No. N00014-91-J-1299, UCLA, August 1993.
  45. J. R. Brockenbrough, R. J. Bucci, A. J. Hinkle, J. Liu, P. E. Magnusen, and S. M. Miyasato, "Role of microstructure on fatigue durability of aluminum aircraft alloys," *Alcoa Report*, Alcoa Laboratories, Alcoa Center, PA 15069, April 1993.
  46. H. C. Hamaker, "Approximating the cumulative normal distribution and its inverse", *Applied Statistics*, 27, pp. 76-79, (1978).



47. S. I. Tomkeieff, "Linear Intercepts, Areas and Volumes", *Nature*, 155, pp. 24, January, (1945).
48. Goodness-of-Fit Techniques, R. B. D'Agostina and M. A. Stephens, Marcel Dekker, Inc, pp. 7-62, 1986.

Table 1. Characteristics of Pores on Different Test Planes and at Different Locations within the 7050-T7451 Plate Alloys

New Pedigree								
Sample	LII (um)	Area%	AR	SI	$\Omega$	Pores/mm <sup>2</sup>	No. of Fields	N
TL, center	3.55	0.114	1.55	0.809	0.109	69.36	234	195
LS, center	3.67	0.199	1.49	0.800	0.478	89.42	215	231
ST, center	3.90	0.136	1.56	0.805	0.392	69.36	240	200
TL, surface	2.91	0.071	1.47	0.831	0.353	64.34	260	201
LS, surface	2.73	0.075	1.52	0.815	0.650	77.17	220	204
ST, surface	3.07	0.075	1.53	0.815	0.546	63.06	260	197
TL, quarter	3.91	0.080	1.52	0.815	0.163	41.61	200	100
LS, quarter	3.50	0.085	1.52	0.823	0.465	54.10	200	130
ST, quarter	4.03	0.093	1.46	0.829	0.270	54.93	200	132
Average	3.47	0.103	1.51	0.816	0.381	64.82	225	177
Old Pedigree								
Sample	LII (um)	Area%	AR	SI	$\Omega$	Pores/mm <sup>2</sup>	No. of Fields	N
TL, center	3.27	0.125	1.50	0.811	0.350	95.71	180	207
LS, center	4.69	0.368	1.45	0.834	0.302	158.68	150	286
ST, center	5.48	0.286	1.51	0.820	0.465	92.94	180	201
TL, surface	3.07	0.071	1.50	0.813	0.147	65.33	200	157
LS, surface	2.48	0.058	1.40	0.845	0.358	76.04	220	201
ST, surface	2.73	0.042	1.41	0.842	0.238	50.73	210	128
TL, quarter	3.07	0.142	1.45	0.834	0.406	130.60	130	204
LS, quarter	2.64	0.042	1.42	0.839	0.345	50.77	200	122
ST, quarter	3.11	0.080	1.41	0.843	0.299	68.66	200	165
Average	3.39	0.135	1.45	0.831	0.323	87.72	186	186

LII - Average intercept length.

AR - Aspect ratio.

SI - Shape index.

$\Omega$  - Orientation factor.

N - Number of detected pores.

Table 2. Parameters of Lognormal Distribution Describing Pore Sizes on Indicated Planes and Locations within the Plate 7050-T7451 Alloys

New Pedigree					
Sample	Fitting Avg.(um)	Std. Dev.	Avg. Conf. 95%	R <sup>2</sup>	N
TL, center	3.26	1.55	0.22	0.9425	195
LS, center	3.04	1.74	0.22	0.9695	231
ST, center	3.65	1.56	0.22	0.9450	200
TL, surface	3.04	1.39	0.19	0.9374	201
LS, surface	2.90	1.38	0.19	0.9033	204
ST, surface	2.23	1.43	0.20	0.8601	197
TL, quarter	3.62	1.53	0.30	0.9293	100
LS, quarter	3.53	1.45	0.25	0.9492	130
ST, quarter	3.18	1.55	0.26	0.8980	132
Average	3.16	1.51	0.23	0.9260	
Old Pedigree					
Sample	Fitting Avg.(um)	Std. Dev.	Avg. Conf. 95%	R <sup>2</sup>	N
TL, center	3.02	1.45	0.20	0.9571	207
LS, center	3.67	1.74	0.20	0.9771	286
ST, center	3.87	1.63	0.23	0.8898	201
TL, surface	2.87	1.37	0.21	0.8738	157
LS, surface	2.61	1.36	0.19	0.9059	201
ST, surface	2.38	1.42	0.25	0.8163	128
TL, quarter	2.69	1.49	0.20	0.8895	204
LS, quarter	2.54	1.40	0.25	0.8369	122
ST, quarter	3.02	1.43	0.22	0.8798	165
Average	2.96	1.48	0.22	0.8918	

N - Number of detected pores.

Table 3. Characteristics of the True 3-D Pore and Constituent Particle Sizes for the 7050-T7451 Plate Alloys

Specimen	Location	a μm	a/b	a/c	R <sub>e</sub>	L <sub>n</sub> ST, Expr	L <sub>n</sub> ST, Simu	L <sub>n</sub> LS, Expr	L <sub>n</sub> LS, Simu	L <sub>n</sub> TL, Expr	L <sub>n</sub> TL, Simu
New Pores	Surface	2.2681 ±1.3641	1.5	1.8	0.063	2.23 ±1.43	2.45 ±1.42	2.90 ±1.38	2.69 ±1.40	3.04 ±1.39	2.73 ±1.40
New Pores	Quarter	2.9083 ±1.4274	1.1	1.8	0.033	3.18 ±1.55	3.30 ±1.51	3.53 ±1.45	3.63 ±1.47	3.62 ±1.53	3.63 ±1.51
New Pores	Center	3.3762 ±1.4105	1.3	1.8	0.100	3.65 ±1.56	3.59 ±1.53	3.04 ±1.74	3.50 ±1.63	3.26 ±1.55	3.86 ±1.49
Old Pores	Surface	2.3562 ±1.3307	1.3	1.8	0.035	2.38 ±1.42	2.45 ±1.39	2.61 ±1.37	2.68 ±1.38	2.87 ±1.37	2.77 ±1.36
Old Pores	Quarter	2.4278 ±1.3440	1.2	1.8	0.074	3.02 ±1.43	2.78 ±1.40	2.54 ±1.40	2.73 ±1.44	2.69 ±1.49	2.89 ±1.44
Old Pores	Center	3.0392 ±1.4485	1.1	1.8	0.135	3.87 ±1.63	3.59 ±1.56	3.67 ±1.74	3.44 ±1.59	3.02 ±1.45	3.80 ±1.54
New Particles	Surface	4.8548 ±1.1486	1.5	3.0	0.066	3.41 ±1.32	3.28 ±1.37	3.78 ±1.36	3.38 ±1.37	3.76 ±1.41	3.47 ±1.43
New Particles	Quarter	4.8796 ±1.3622	1.5	2.8	0.084	4.07 ±1.44	3.91 ±1.45	4.29 ±1.47	3.73 ±1.43	4.13 ±1.42	4.17 ±1.51
New Particles	Center	6.8178 ±1.2740	1.5	3.0	0.139	3.45 ±1.65	4.32 ±1.63	5.10 ±1.50	4.46 ±1.61	5.30 ±1.73	5.06 ±1.54
Old Particles	Surface	4.4831 ±1.3398	1.5	3.0	0.068	3.34 ±1.41	3.50 ±1.43	4.01 ±1.39	3.34 ±1.41	4.07 ±1.44	3.76 ±1.47
Old Particles	Quarter	5.5158 ±1.3951	1.5	2.8	0.063	4.62 ±1.58	4.04 ±1.55	4.18 ±1.52	4.35 ±1.59	4.74 ±1.68	4.79 ±1.65
Old Particles	Center	7.2855 ±1.2847	2.5	2.5	0.069	3.81 ±1.55	4.03 ±1.63	5.80 ±1.69	5.02 ±1.68	5.27 ±1.63	4.59 ±1.64

a - Largest ellipsoid radius.

a/b, a/c - Aspect ratios.

R<sub>e</sub> - Parameter describing goodness of fit.

L<sub>n</sub> - Average size on indicated planes (μm).

**Table 4. Characteristics of Constituent Particles on Different Test Planes and at Different Locations within the 7050-T7451 Plate Alloys**

New Pedigree								
Sample	LII (um)	Area%	AR	SI	$\Omega$	Ptcls/mm <sup>2</sup>	No. of Fields	N
TL, center	6.20	0.542	1.78	0.748	0.224	94.32	180	204
LS, center	4.84	0.480	2.35	0.663	0.754	69.29	215	179
ST, center	3.71	0.845	2.27	0.663	0.586	297.77	90	322
TL, surface	3.44	1.125	2.34	0.674	0.432	509.76	40	245
LS, surface	3.35	0.745	2.41	0.652	0.741	371.19	50	223
ST, surface	2.97	0.458	2.05	0.712	0.532	295.45	60	213
TL, quarter	3.72	0.350	2.33	0.671	0.169	140.79	120	203
LS, quarter	4.13	0.638	2.48	0.659	0.706	216.39	80	208
ST, quarter	3.77	0.349	2.53	0.646	0.546	135.72	130	212
Average	4.01	0.615	2.28	0.676	0.521	236.74	107	223
Old Pedigree								
Sample	LII (um)	Area%	AR	SI	$\Omega$	Ptcls/mm <sup>2</sup>	No. of Fields	N
TL, center	6.14	0.629	2.06	0.704	0.412	94.32	180	204
LS, center	6.38	0.524	2.36	0.655	0.698	66.91	250	201
ST, center	4.57	0.907	1.62	0.790	0.560	327.36	60	236
TL, surface	4.04	0.746	1.71	0.769	0.318	328.01	51	201
LS, surface	3.64	0.545	1.90	0.736	0.632	254.43	70	214
ST, surface	3.12	0.453	1.76	0.760	0.348	303.78	60	219
TL, quarter	5.67	0.839	1.78	0.761	0.148	186.80	90	202
LS, quarter	4.38	0.708	1.77	0.761	0.288	249.68	70	210
ST, quarter	4.99	0.931	1.87	0.747	0.446	252.06	70	212
Average	4.77	0.698	1.87	0.743	0.428	229.26	100	211

LII - Average intercept length.

AR - Aspect ratio.

SI - Shape index.

$\Omega$  - Orientation factor.

N - Number of detected particles.

**Table 5. Parameters of Lognormal Distribution Describing Constituent Particle on Indicated Planes and Locations within the Plate 7050-T7451 Alloys**

New Pedigree					
Sample	Fitting Avg.(um)	Std. Dev.	Avg. Conf. 95%	R^2	N
TL, center	5.30	1.73	0.24	0.9885	204
LS, center	5.10	1.50	0.22	0.6633	179
ST, center	3.45	1.65	0.18	0.6627	322
TL, surface	3.76	1.41	0.18	0.9151	245
LS, surface	3.78	1.36	0.18	0.8964	223
ST, surface	3.41	1.32	0.18	0.9076	213
TL, quarter	4.13	1.42	0.20	0.9215	203
LS, quarter	4.29	1.47	0.20	0.9408	208
ST, quarter	4.07	1.44	0.19	0.9408	212
Average	4.14	1.48	0.20	0.8707	
Old Pedigree					
Sample	Fitting Avg.(um)	Std. Dev.	Avg. Conf. 95%	R^2	N
TL, center	5.27	1.63	0.22	0.9611	204
LS, center	5.80	1.69	0.23	0.9926	201
ST, center	3.81	1.55	0.20	0.9588	236
TL, surface	4.07	1.44	0.20	0.9556	201
LS, surface	4.01	1.39	0.19	0.9641	214
ST, surface	3.34	1.41	0.19	0.9312	219
TL, quarter	4.74	1.68	0.23	0.9428	202
LS, quarter	4.18	1.52	0.21	0.9282	210
ST, quarter	4.62	1.58	0.21	0.9296	212
Average	4.43	1.54	0.21	0.9516	

N - Number of detected particles.

**Table 6. Results of the Tessellation Analysis for Pores and Constituent  
Particles in the Old Pedigree 7050-T7451 Plate Alloy  
(ST Plane, Center Section)**

Pores						
	Average	Minimum	Maximum	St. Dev.	Geom. Av.	Median
Near-Neighb. ( $\mu\text{m}$ )	114	2.83	324	65.3	91.5	116
Nearest-Nbr. ( $\mu\text{m}$ )	48.2	2.83	156	33.2	35	42.5
Local V.F. %	.00502	.000129	0.156	.0141	.00168	.00146
Particle Area ( $\mu\text{m}^2$ )	30.8	2.3	520	61.9	14.1	11.7
Cell Area ( $\text{mm}^2$ )	.0108	.000439	.033	.00714	.00842	.00952
Cell Sides No.	5.74	3	15			
Particles						
	Average	Minimum	Maximum	St. Dev.	Geom. Av.	Median
Near-Neighb. ( $\mu\text{m}$ )	58.0	1.0	194	38.2	44.0	66.6
Nearest-Nbr. ( $\mu\text{m}$ )	25.2	1.0	119	19.2	17.9	21.3
Local V.F. %	.0413	.000262	4.38	.292	.007	.00628
Particle Area ( $\mu\text{m}^2$ )	27.8	3.00	266	44.5	14.8	12.2
Cell Area ( $\text{mm}^2$ )	.0033	.000029	.0216	.0034	.0021	.0022
Cell Sides No.	5.76	3	15			

Table 7. Values of Q and R for Pore and Particle Distributions in 7050-T7451 Plate Alloy

Specimen	Q	R	L	H	N	NND_obs	STD_obs	NND_rdm	STD_rdm	Spatial Distribution type
new pores, TL, center	0.9231	1.2636	1908	1417	189	55.2	39.5	59.8017	31.2595	Random with clusters
new pores, LS, center	0.8570	1.4605	5470	472	226	45.8	40.8	53.4417	27.9351	Random with clusters
new pores, ST, center	0.9328	1.2103	1900	1600	200	57.5	39.0	61.6441	32.2226	Random with clusters
new particles, TL, center	0.6791	1.2734	1908	1133	200	35.3	34.6	51.9827	27.1724	Random with clusters
new particles, LS, center	0.6626	1.1596	5470	472	178	39.9	36.5	60.2178	31.4770	Random with clusters
new particles, ST, center	0.8143	1.1379	1908	378	226	23.0	16.8	28.2456	14.7645	Random with clusters
old, pores, TL, center	0.8670	1.3029	1908	1133	207	44.3	34.8	51.0962	26.7090	Random with clusters
old, pores, LS, center	0.8920	1.0156	1272	944	218	33.1	19.7	37.1083	19.3973	Random with clusters
old, pores, ST, center	0.9294	1.2247	1272	1700	201	48.2	33.2	51.8609	27.1087	Random with clusters
old, particles, TL, center	0.5720	1.0794	1908	1133	206	29.3	28.9	51.2201	26.7738	Random with clusters
old, particles, LS, center	0.7389	1.3328	1272	2361	198	45.5	42.9	61.5785	32.1883	Random with clusters
old, particles, ST, center	0.9117	1.3289	1272	567	236	25.2	19.2	27.6407	14.4483	Random with clusters

L, H - Length and height of the field in  $\mu\text{m}$ .

NND - Nearest Neighbor Distance.

STD - Standard Deviation.

N - Number of detected features

rdm - Random distribution.

new, old - New and old pedigree alloys.

obs - Experimental



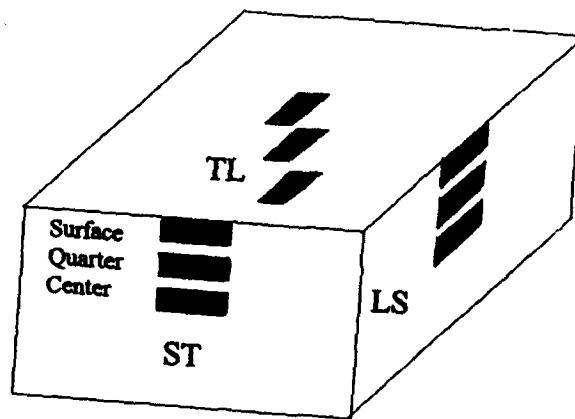


Figure 1. Locations of the metallographic test planes in the 7050-T7451 Al plate alloys.

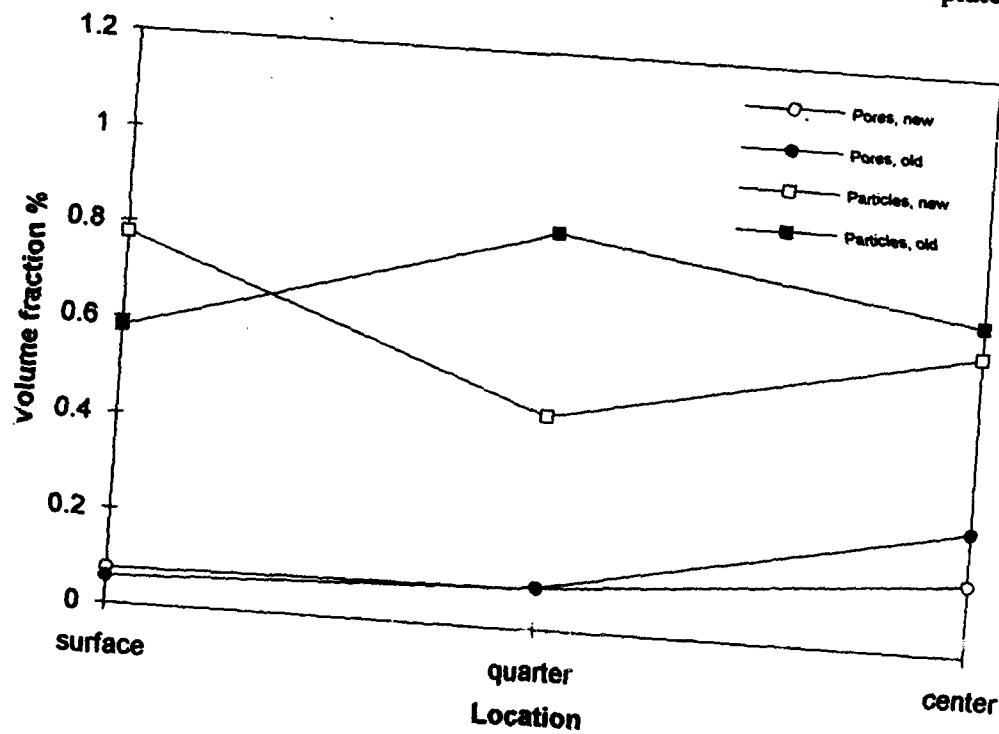


Figure 2. Average volume fractions of pores and particles at different plate locations for both old and new 7050-T7451 alloys.

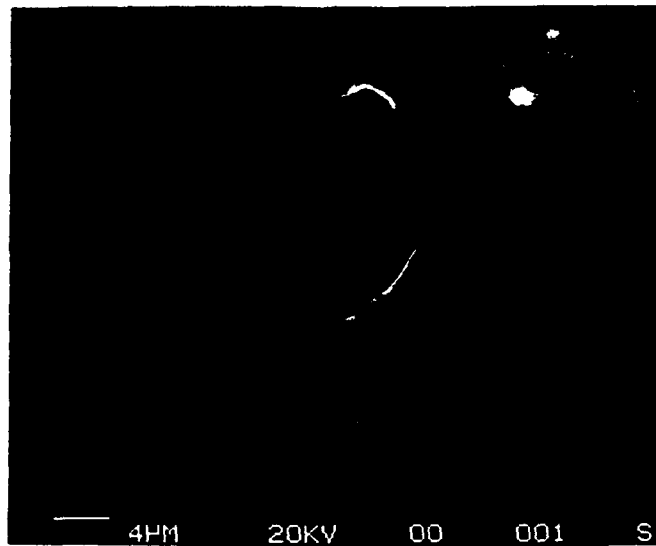


Figure 3. A typical pore in the 7050-T7451 plate alloy.

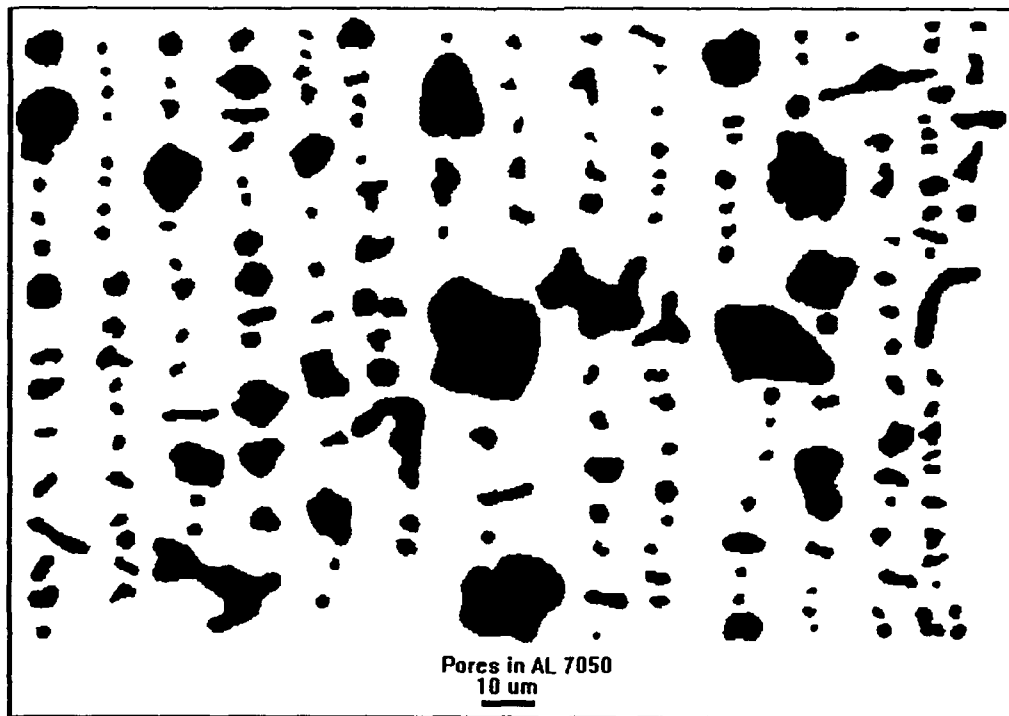


Figure 4. A collection of 201 pores found on the ST-planes, center region, old 7050-T7451 plate alloy. Pores were collected from 180 micrographs.

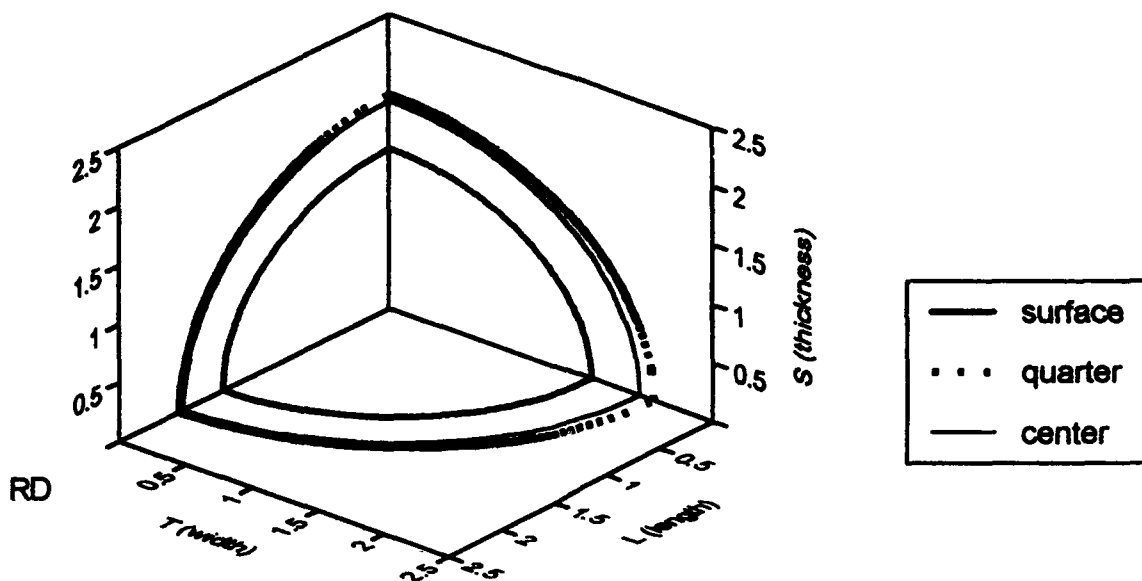


Figure 5. The average pore intercept lengths for the new pedigree 7050-T7451 plate alloy as a function of direction at the surface, quarter depth and center of the plate.

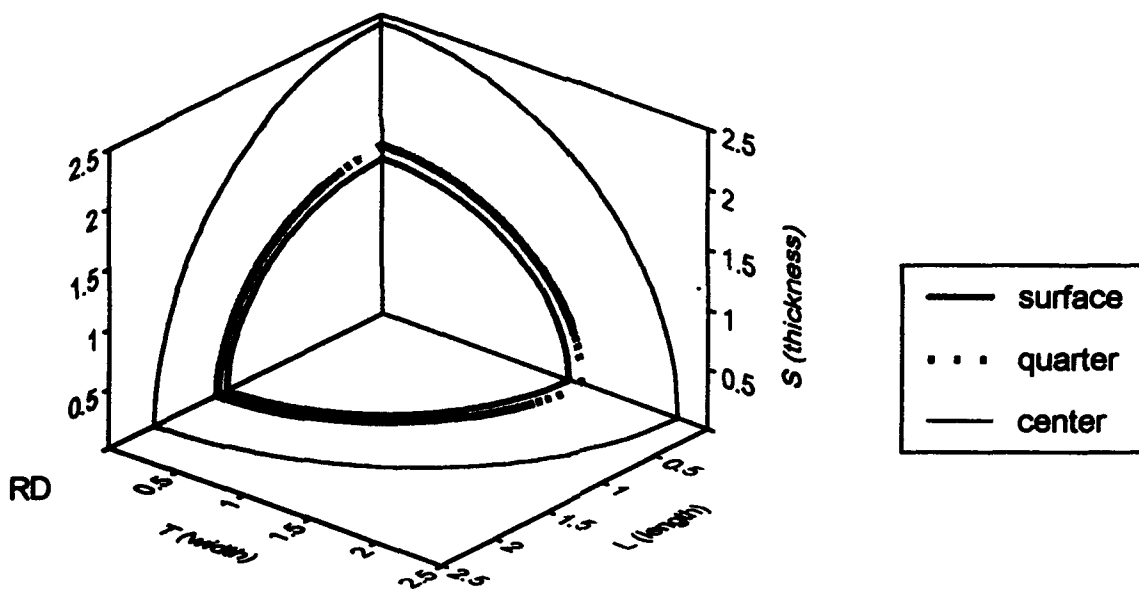


Figure 6. The average pore intercept lengths for the old pedigree 7050-T7451 plate alloy as a function of direction at the surface, quarter depth and center of the plate.

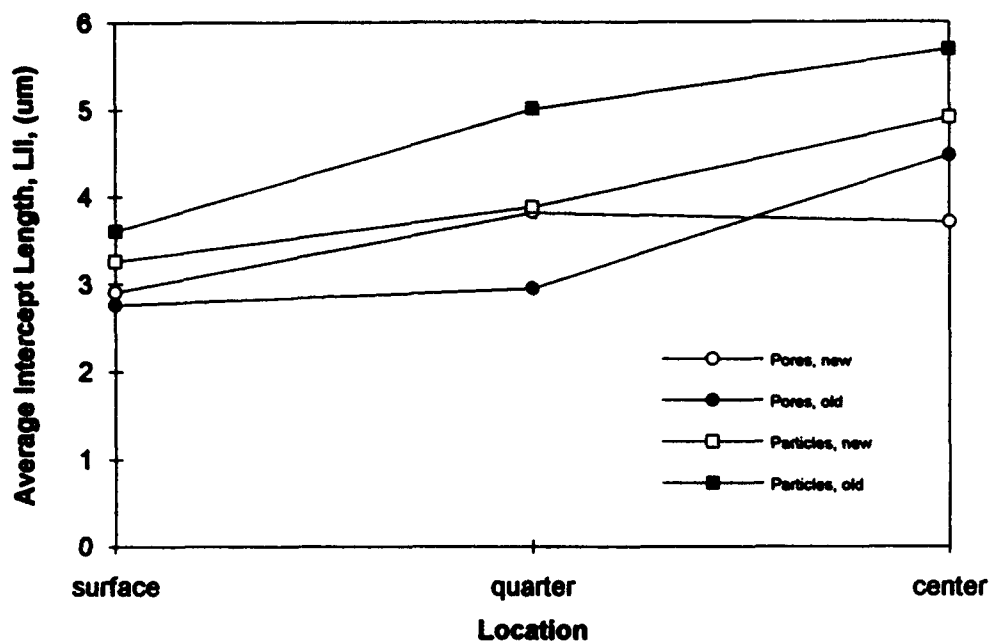


Figure 7. Average intercept length,  $L_{II}$ , for pores and particles at different plate locations for the old and new 7050-T7451 plate alloys.

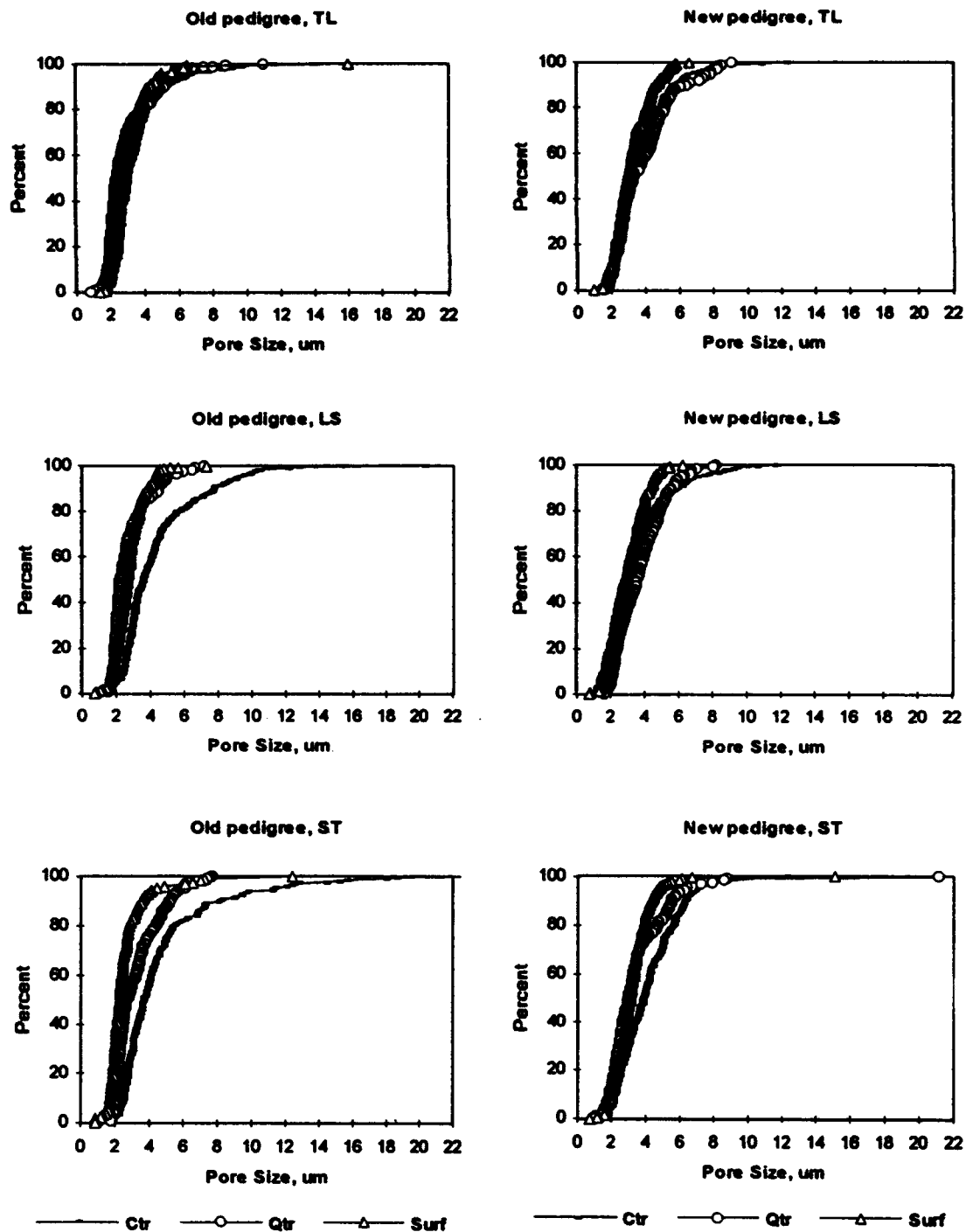


Figure 8. Cumulative 2-D pore size distributions for the 7050-T7451 plate alloys.

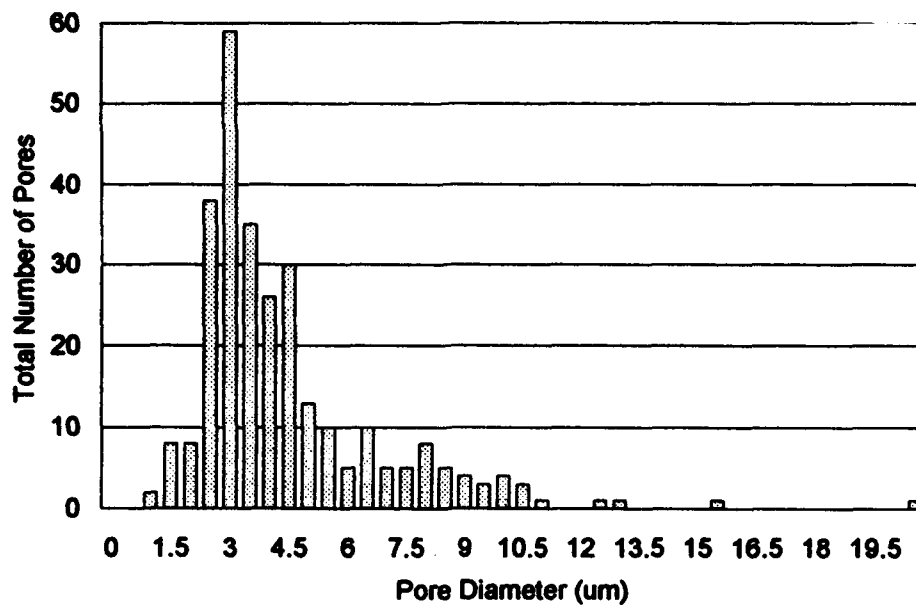


Figure 9. An example of the pore size distribution on LS plane, center region, old 7050-T7451 plate alloy.

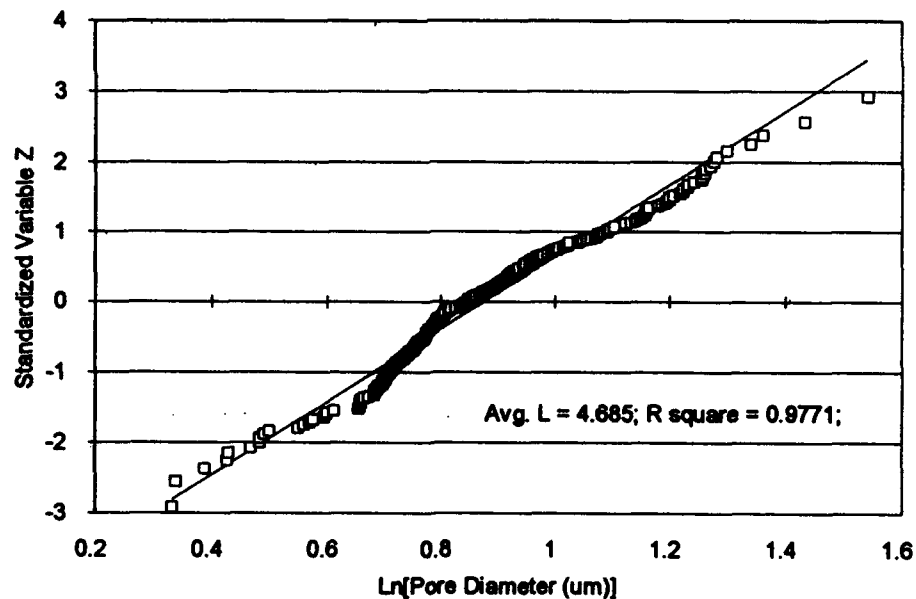


Figure 10. An example of the fit of the lognormal distribution to the pore size data; LS plane, center region, old 7050-T7451 plate alloy. Solid line represents lognormal distribution and open squares are the experimental data.

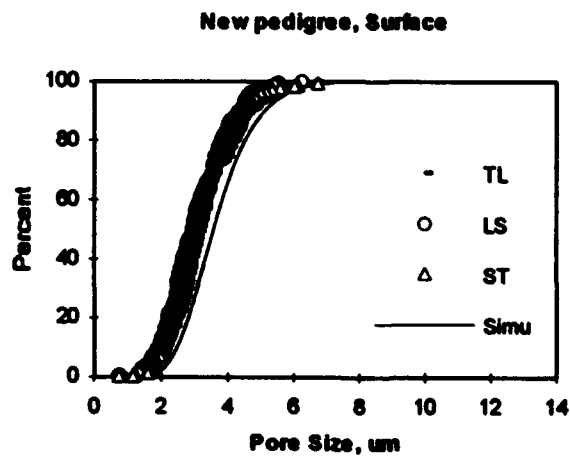
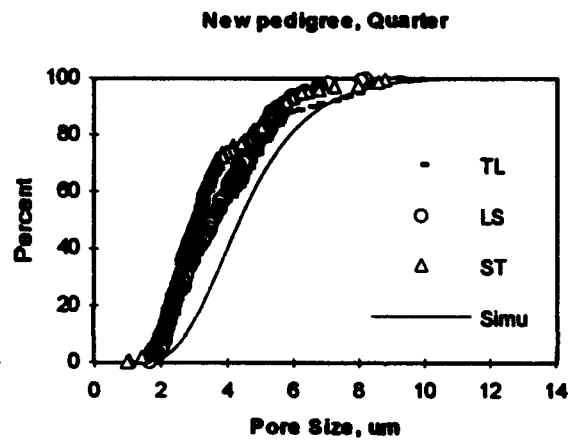
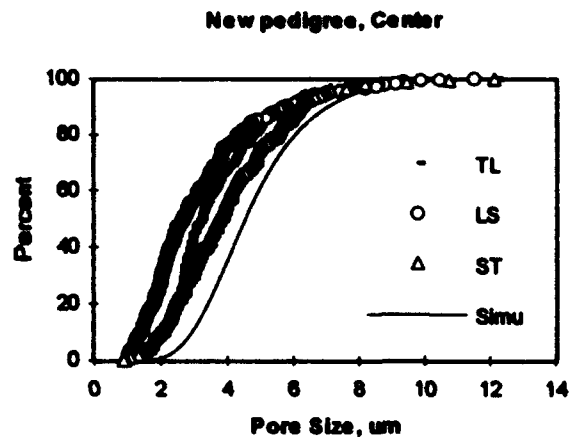


Figure 11. Experimental, 2-D, and estimated 3-D cumulative pore size distributions in the new pedigree 7050-T7451 plate alloy.

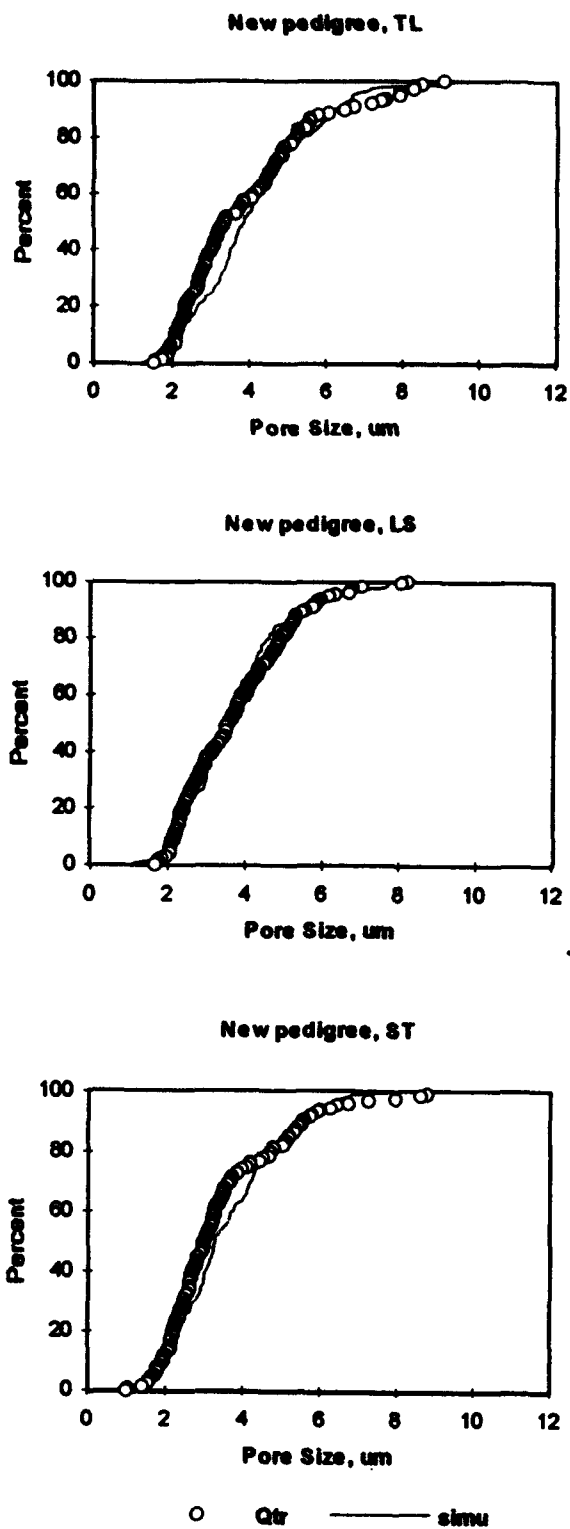


Figure 12. Comparison of the experimental and simulated cumulative 2-D pore size distributions in the new pedigree 7050-T7451 plate alloy.



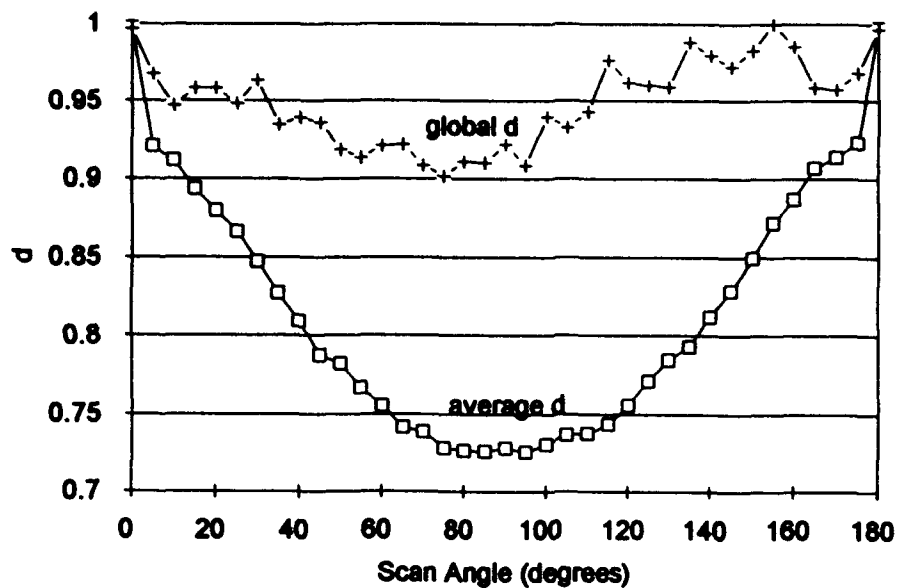


Figure 13. The angular variation of the normalized average intercept lengths for the pores in the old pedigree 7050-T7451 plate alloy, on ST plane, center region. See text for definitions of global and average d's.

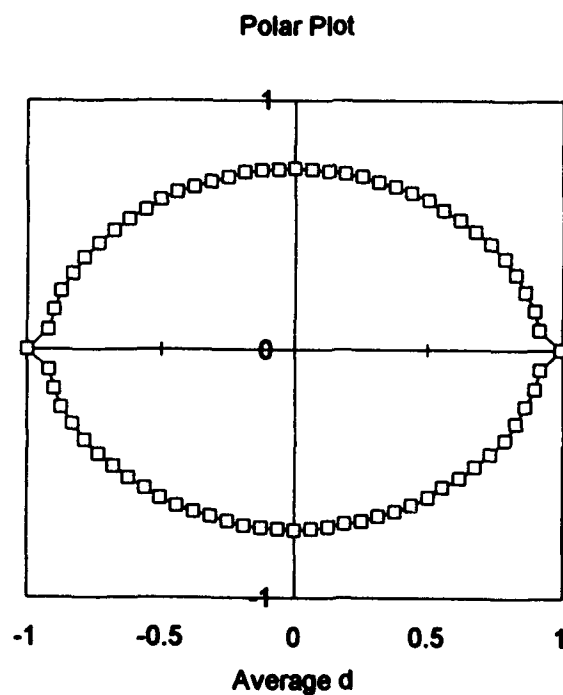


Figure 14. The normalized average  $d$  of the pores plotted in polar coordinates. The polar plot gives a direct visual representation of the pore shapes.

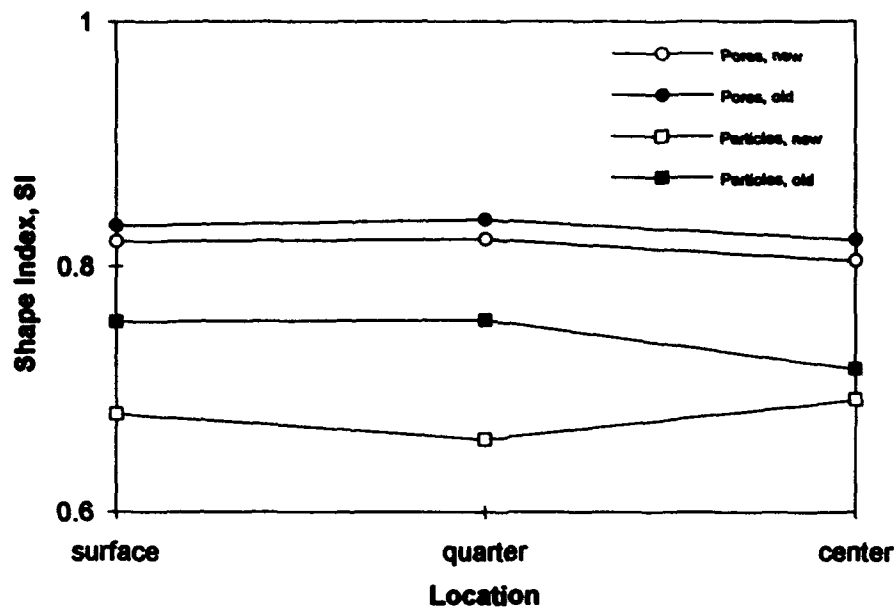


Figure 15. Average shape indexes, SI, for the pores and particles at different plate locations for both old and new pedigree 7050-T7451 plate alloys.

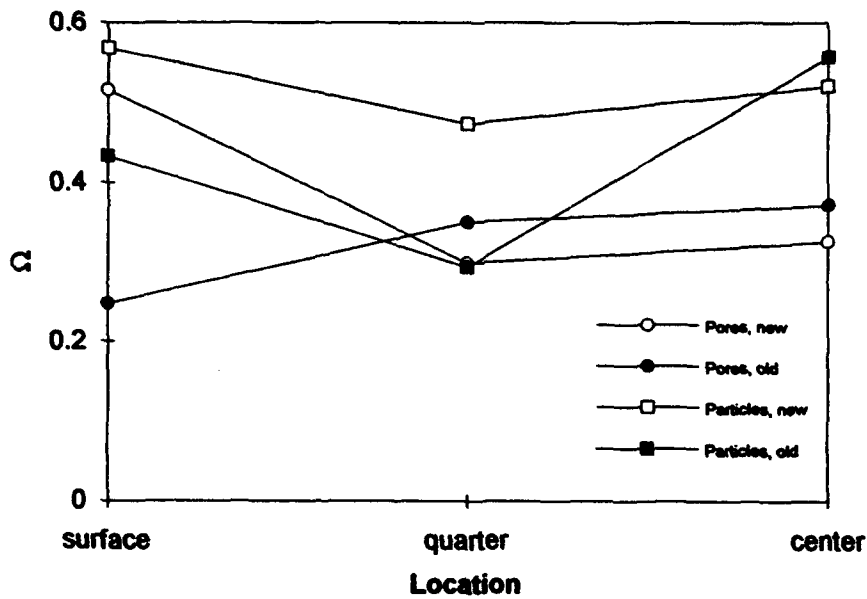


Figure 16. Average orientation factors,  $\Omega$ , for the pores and particles at different plate locations for both old and new pedigree 7050-T7451 plate alloys.

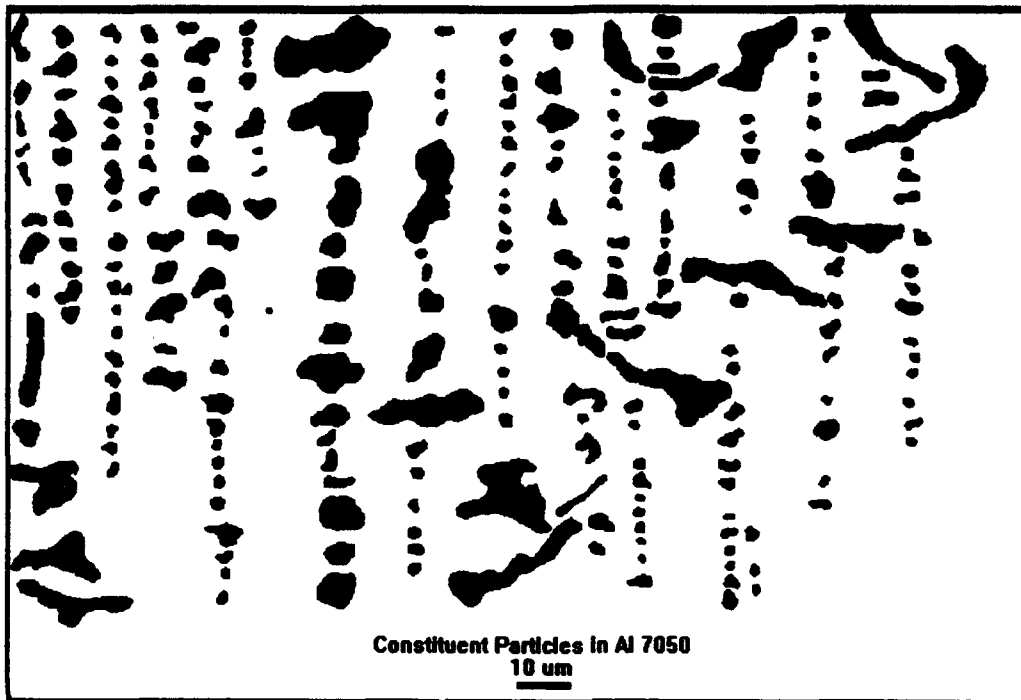


Figure 17. A collection of 236 constituent particles found on ST plane, center region of the old pedigree 7050-T7451 Al plate alloy. Particles were collected from 60 micrographs.

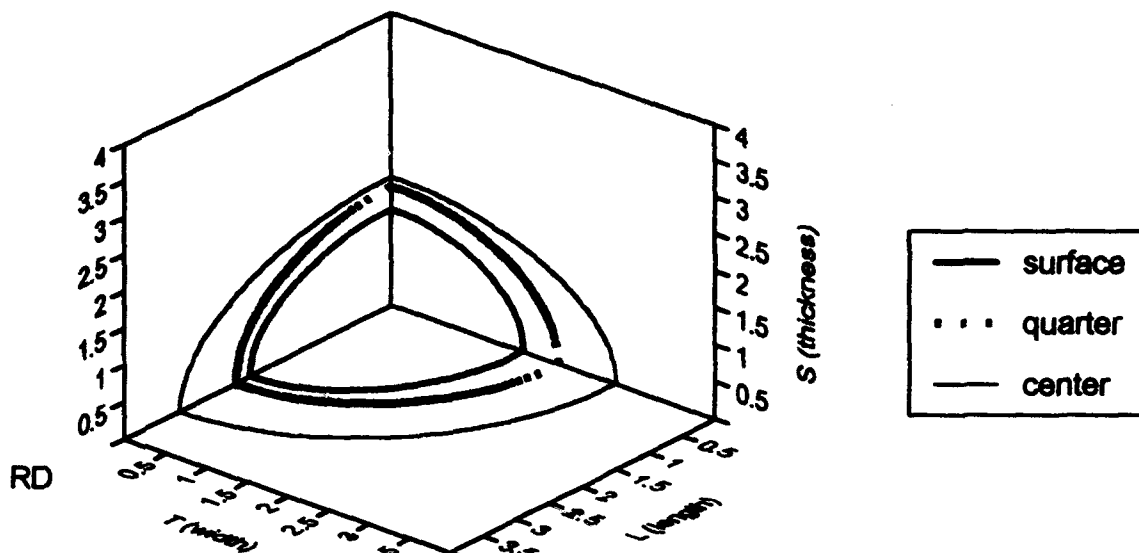


Figure 18. The average particle intercept lengths for the new pedigree 7050-T7451 plate alloy as a function of direction at the surface, quarter depth and center of the plate.

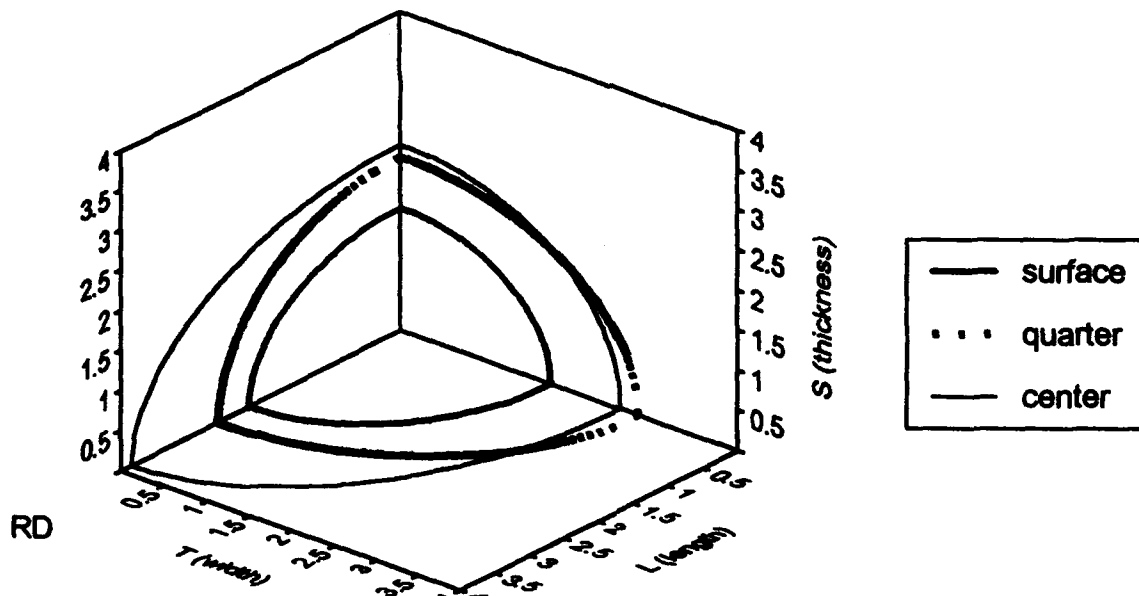


Figure 19. The average particle intercept lengths for the old pedigree 7050-T7451 plate alloy as a function of direction at the surface, quarter depth and center of the plate.

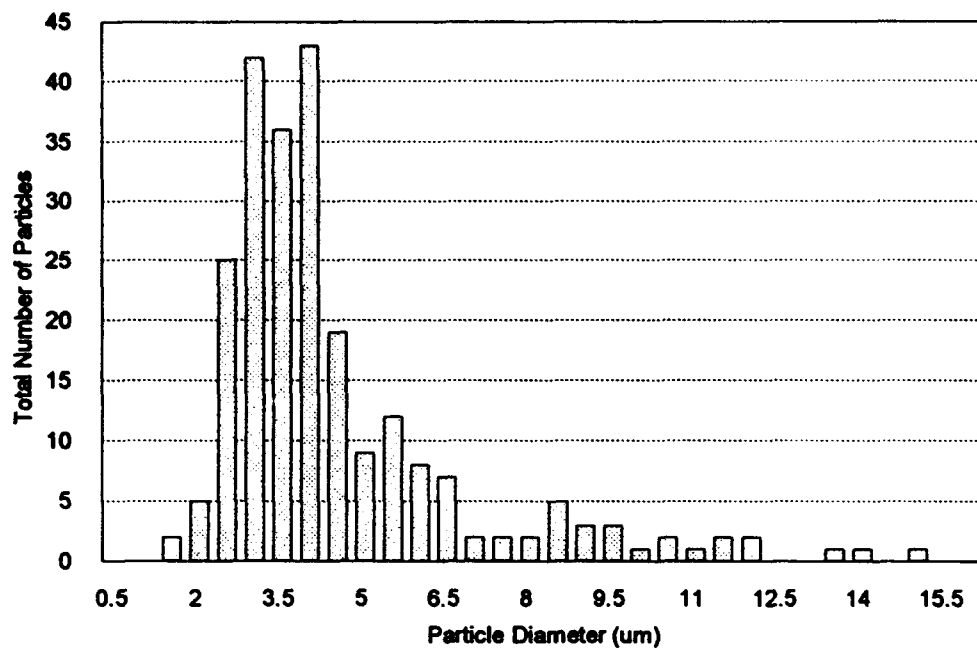


Figure 20. An example of the size distribution of the constituent particles on ST plane, center region of the old pedigree 7050-T7451 Al plate alloy.

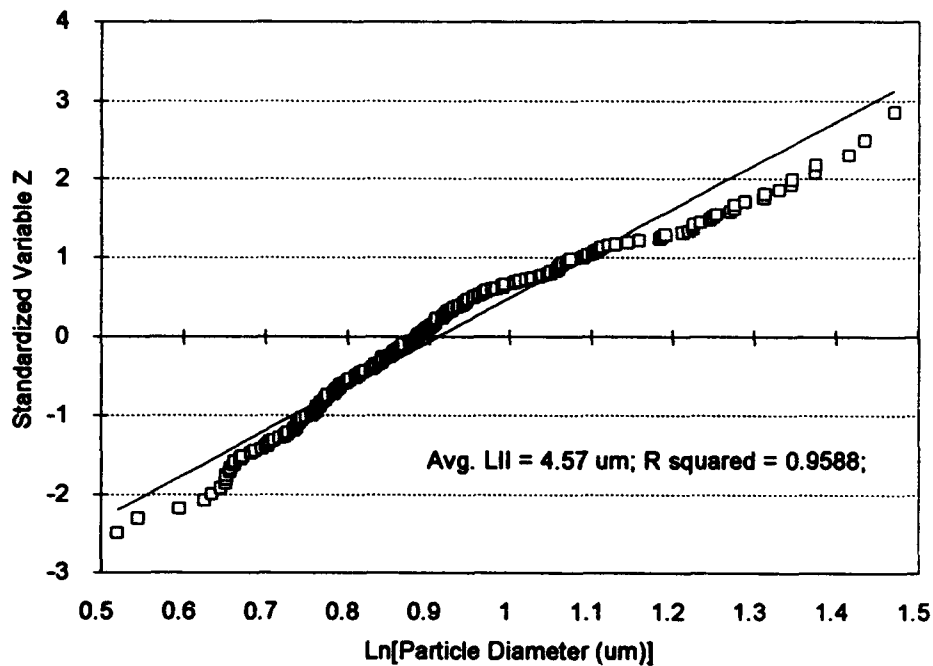


Figure 21. An example of the fit of the lognormal distribution to the particle size data; ST plane, center region, old pedigree 7050-T7451 Al plate alloy. Solid line represents the lognormal distribution and open squares are the experimental data.

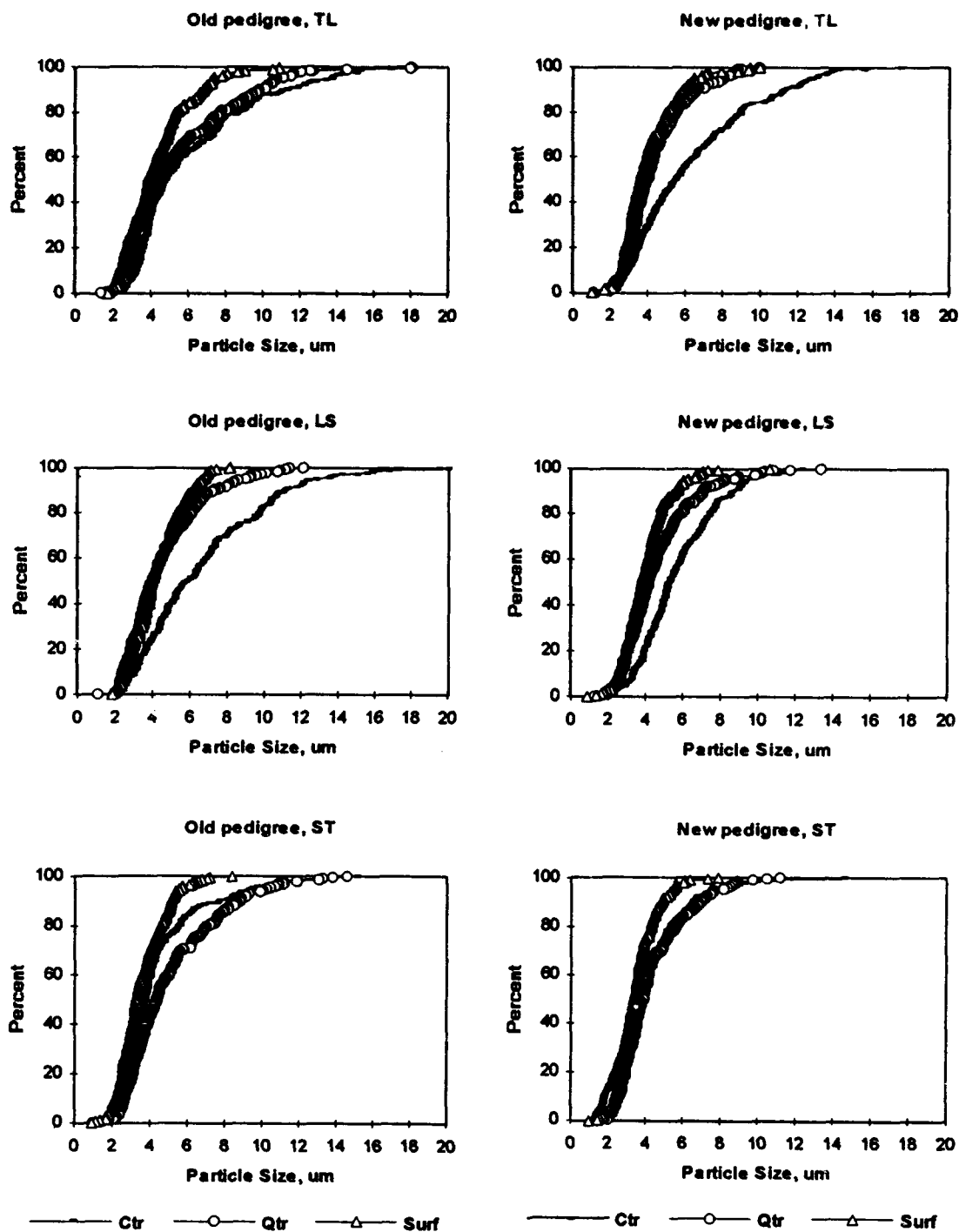


Figure 22. Cumulative 2-D particle size distributions for the 7050-T7451 plate alloy.

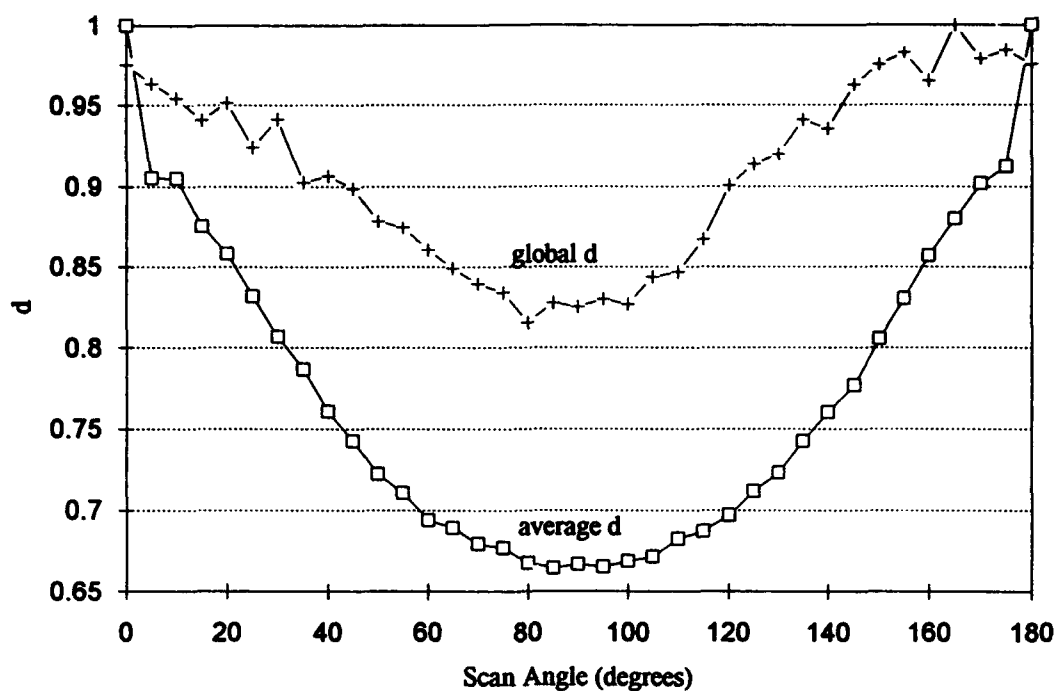


Figure 23. The average variation of the normalized average intercept lengths for the constituent particles shown in Fig. 17. See text for definitions of global and average  $d$ 's.

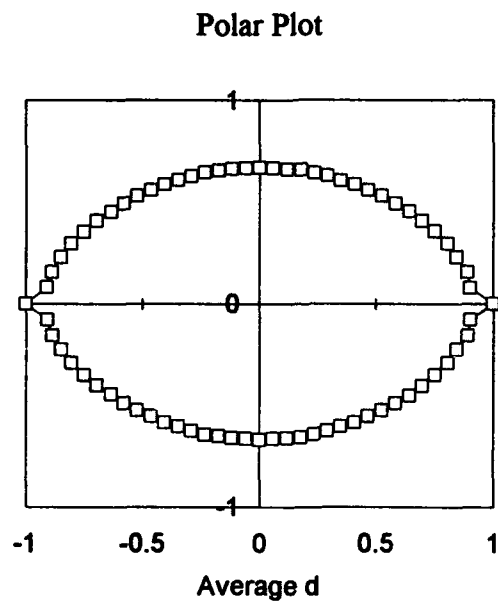


Figure 24. The normalized average  $d$  for the constituent particles in Fig. 17 plotted in polar coordinates. The polar plot gives a direct visual representation of the particle shapes.



Pores in Al 7050  
200  $\mu$ m

Figure 25. The Dirichlet tessellation cells constructed on the pore centers; ST plane, center region, old pedigree 7050-T7451 plate alloy. Points represent locations of pore centers.

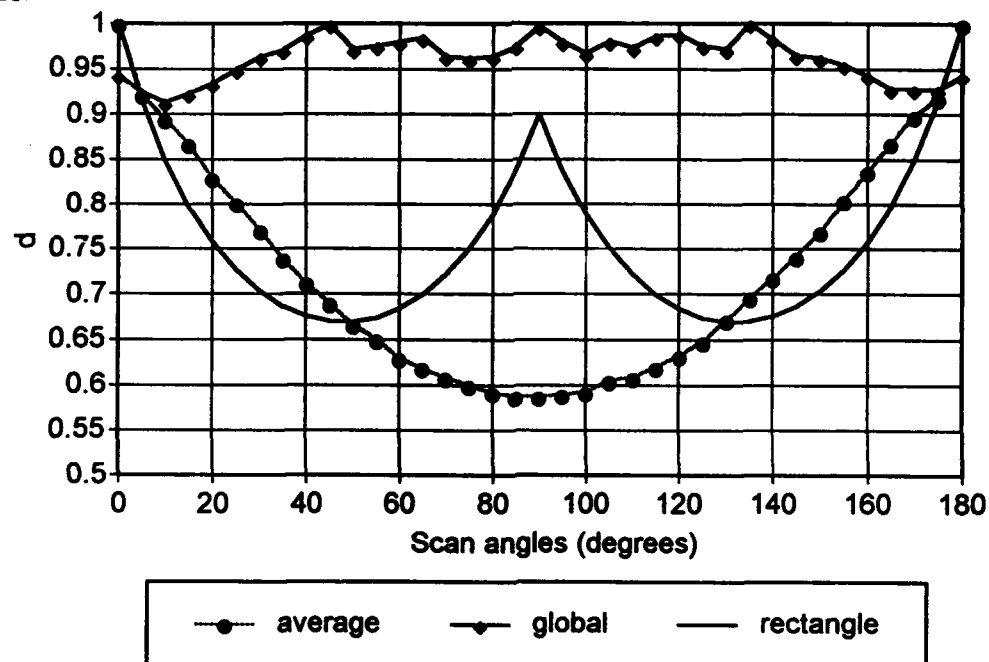


Figure 26. The normalized average intercept lengths of the tessellation cells constructed for the pores. The  $d-\alpha$  curves for a rectangular and random point patterns are shown for comparison.



**END  
FILMED**

DATE: 9-94

**DTIC**